

Last edited: November 10, 2018

SPATIAL ANALYSIS OF THE H α EMISSION IN THE LOCAL STAR-FORMING UCM GALAXIES

Pablo G. Pérez-González¹, Jaime Zamorano and Jesús Gallego

Departamento de Astrofísica, Facultad de Físicas, Universidad Complutense, E-28040 Madrid, Spain

Alfonso Aragón-Salamanca

School of Physics and Astronomy, University of Nottingham, NG7 2RD, UK

and

Armando Gil de Paz

The Observatories of the Carnegie Institution of Washington, 813 Santa Barbara St., Pasadena, CA 91101, USA

ABSTRACT

We present a photometric study of the H α emission in the *Universidad Complutense de Madrid* (UCM) Survey galaxies. This work complements our previously-published spectroscopic data. We study the location of the star-forming knots, their intensity, concentration, and the relationship of these properties with those of the host galaxy. We also estimate that the amount of H α emission that arises from the diffuse ionized gas is about 15–30% of the total H α flux for a typical UCM galaxy. This percentage seems to be independent of the Hubble type. Conversely, we found that an ‘average’ UCM galaxy harbours a star formation event with 30% of its H α luminosity arising from a nuclear component. The implications of these results for higher-redshift studies are discussed, including the effects of galaxy size and the depth of the observations. A correlation between the SFR and the Balmer decrement is observed, but such correlation breaks down for large values of the extinction. Finally, we recalculate the H α luminosity function and star formation rate density of the local Universe using the new imaging

¹pag@astrax.fis.ucm.es

data. Our results point out that, on average, spectroscopic observations detected about one third of the total emission-line flux of a typical UCM galaxy. The new values obtained for the $H\alpha$ luminosity density and the star formation rate density of the local Universe are $10^{39.3\pm 0.2} \text{ erg s}^{-1} \text{ Mpc}^{-3}$, and $\rho_{SFR} = 0.016_{-0.004}^{+0.007} \mathcal{M}_{\odot} \text{ yr}^{-1} \text{ Mpc}^{-3}$ ($H_0 = 50 \text{ km s}^{-1} \text{ Mpc}^{-1}$, $\Omega_M = 1.0$, $\Lambda = 0$). The corresponding values for the ‘concordance cosmology’ ($H_0 = 70 \text{ km s}^{-1} \text{ Mpc}^{-1}$, $\Omega_M = 0.3$, $\Lambda = 0.7$) are $10^{39.5\pm 0.2} \text{ erg s}^{-1} \text{ Mpc}^{-3}$ $\rho_{SFR} = 0.029_{-0.005}^{+0.008} \mathcal{M}_{\odot} \text{ yr}^{-1} \text{ Mpc}^{-3}$.

Subject headings: surveys — galaxies: starburst — galaxies: fundamental parameters — galaxies: photometry — galaxies: stellar content

1. Introduction

The characterization of the star formation in galaxies at any cosmic epoch remains a topic of considerable interest (see, e.g., Yan et al. 1999; Haarsma et al. 2000; Somerville et al. 2001; Rowan-Robinson 2001; Lanzetta et al. 2002). Much effort has been devoted to the study of star-forming galaxies at low, intermediate, and high redshift in the last decade (among others, Songaila et al. 1994; Gallego et al. 1995; Lilly et al. 1996; Ellis et al. 1996; Hogg et al. 1998; Jones & Bland-Hawthorn 2001; Pettini et al. 2001; Pascual et al. 2001; Tresse et al. 2001). These studies have revealed that the comoving star formation rate (SFR) density of the Universe has increased by an order of magnitude from the present time to $z \sim 1 - 2$. The behavior beyond redshift $z \sim 2$ is still an open issue, with some results indicating a declining SFR with redshift, while others suggest little or no evolution.

If we want to understand how the star-formation process has evolved with time, the statistical determination of the star formation history of the Universe as a whole needs to be complemented with the characterization of the star-formation properties of the individual galaxies. This is not an easy task for high- z objects, given their small angular size and faintness, but some progress is being made. Complementary studies of local samples of star-forming galaxies are also clearly needed for comparison purposes, and to provide information on the end-point of the evolution. Thus, detailed analysis of the spatial distribution and intensity of the star formation in local galaxies may have important implications for studies at intermediate and high redshifts. Though evolution certainly plays an important role when studying galaxies at different redshifts, some properties may remain comparable and easily measurable (Gallego 1998; Conselice et al. 2000a). Several authors have found similarities between local and distant objects in size (Pérez-González et al. 2001), intensity of the starburst (Meurer et al. 1997), relationship between the newly-formed stars and the population of more evolved stars (Pérez-González et al. 2003b), stellar mass (Kauffmann et al. 2002),

etc. In addition, much work is now focusing on the characterization of local counterparts of distant objects (e.g., the Luminous Blue Compact Galaxies in Guzmán et al. 1997 and Pisano et al. 2001, or the UV-bright starburst galaxies in Conselice et al. 2000b).

Kennicutt (1983) carried out pioneering work on the study of the structural properties of the recent star formation in normal disk galaxies. This work made use of the $H\alpha + [N\ II]$ nebular emission as a tracer of the population of young hot stars (responsible for the heating of the gas). Similar papers have gone deeper into the issue, following a variety of approaches: (1) comparing the rate of star formation with other properties such as the morphology, the gas content or the older stellar population content (Kennicutt et al. 1994; Kennicutt 1998b); (2) shedding light on the influence of the environment on star formation by studying samples of field galaxies, compact groups, and clusters (Gavazzi et al. 1998; Iglesias-Páramo & Vílchez 1999; Hameed & Devereux 1999); (3) extending the analysis to galaxies with enhanced star formation (Conselice et al. 2000b; Chitre & Joshi 2001). These studies demonstrate that the use of $H\alpha$ photometry can be extremely useful in the characterization of the youngest stellar population in star-forming galaxies, and in complementing spectroscopic observations.

Another interesting topic outlined relatively recently is the amount of $H\alpha$ emission arising from the *diffuse ionized gas* (DIG) of galaxies (Reynolds 1990). The DIG has been studied in nearby normal spiral galaxies with high angular resolution (see, e.g., Lehnert & Heckman 1994; Hoopes et al. 2001; Zurita et al. 2002). The ionizing source of this interstellar medium component is still uncertain: some authors identify it with young hot stars in HII regions, while others introduce new possibilities such as supernova remnants, turbulent mixing layers or even the extragalactic radiation field (Wang et al. 1997). If the link between the DIG and the HII regions is confirmed, models should account for the escape of a non-negligible fraction of ionizing Lyman photons, which could reach the intergalactic medium. This effect, if confirmed, would imply that the factor used when converting from $H\alpha$ luminosity to star formation rate could be underestimated (see Kennicutt 1998a, and references therein).

In this paper we present $H\alpha$ imaging observations for a complete sample of local star-forming objects: the *Universidad Complutense de Madrid* (UCM) Survey galaxies (Zamorano et al. 1994, 1996; Alonso et al. 1999). These galaxies present enhanced star formation in comparison with normal quiescent spiral galaxies (Gil de Paz et al. 2000; Pérez-González et al. 2003a,b). A comparison of the UCM Survey galaxies with distant objects has been carried out for different properties, including size, total luminosity (Pérez-González et al. 2000), mass, and intensity of the star formation episode (Pérez-González et al. 2003b). This sample has often been used as the local benchmark for intermediate and high redshift studies (see, for example, Madau et al. 1998).

The UCM galaxies have been extensively observed in optical and near infrared photo-

metric passbands (Vitores et al. 1996a; Gil de Paz et al. 2000; Pérez-González et al. 2000; Pérez-González et al. 2003a). Optical long-slit spectroscopy (Gallego et al. 1996) is also available for the entire sample. The latter study allowed to obtain emission-line fluxes and ratios, yielding results on star formation rates (via $H\alpha$ fluxes), extinctions (through the Balmer decrement), metallicities (using oxygen abundances), etc. However, these observations suffer from the effect of the finite aperture of the slit and the consequent loss of spatial information. In this sense, spectroscopic observations (commonly centered in the galaxy nucleus²) may have missed large HII regions in the outer disk zones. In addition, when aperture corrections are applied, a strongly emitting nucleus may cause the integrated emission to be largely overestimated. The $H\alpha$ imaging data presented in this paper complement the spectroscopic observations, providing information about the location of the star-forming knots, their intensity and relationship with the host galaxy where the starburst is taking place. In addition, an estimate of the DIG emission will be measured for a complete sample of star-forming galaxies.

This paper is structured as follows. Section 2 presents the sample of galaxies and observations used in this work. Next, Section 3 discusses on the results concerning the comparison between imaging and spectroscopy, the concentration and size properties, the DIG characterization, the implications for studies at higher redshifts, and the corrections to the local $H\alpha$ luminosity function and star formation rate density. Unless otherwise indicated, throughout this paper we use a cosmology with $H_0 = 70 \text{ km s}^{-1} \text{ Mpc}^{-1}$, $\Omega_M = 0.3$ and $\Lambda = 0.7$.

2. The sample

The *Universidad Complutense de Madrid* (UCM) Survey for emission-line galaxies was carried out in the late 1980s and early 1990s with two main goals: (1) characterizing the star formation in the local Universe, and (2) studying low metallicity objects (Zamorano et al. 1994, Lists I; Zamorano et al. 1996, List II; and Alonso et al. 1999, List III). Extensive imaging and spectroscopic follow-up observations are available for the vast majority of the galaxies in the sample.

Long-slit spectroscopy for the UCM galaxies was presented in Gallego et al. (1996, 1997). The mean redshift of the complete sample of 191 emission-line galaxies is 0.026. The sample is dominated (57%) by objects with low excitation, relatively high metallicity, and often

²In this paper we will refer to the starbursts in the inner parts of spirals aside nuclear activity as nuclear star formation.

bright and dusty nuclear starbursts. We call these *disk-like* galaxies. A significant number of high excitation, low metallicity galaxies are also present (32%), and we call them *HII-like* galaxies. These have blue star-forming knots which may sometimes dominate the optical luminosity of the whole galaxy, as in the case of *Blue Compact Galaxies* (BCDs). A number of AGNs (8%) was also detected. For the remaining 3% it was not possible to obtain a spectroscopic classification. The spectroscopic data were also used to obtain the luminosity function and star formation rate density of the local Universe (Gallego et al. 1995, 2002).

Imaging and photometric studies in the Gunn-*r* (Vitores et al. 1996a,b) and Johnson-*B* bands (Pérez-González et al. 2000, 2001) have also been carried out. The average magnitudes of the sample are $m_B = 16.1 \pm 1.1$ ($M_B = -19.2$) and $m_r = 15.5 \pm 1.0$ ($M_r = -19.8$), with a mean effective radius of 2.8 kpc (in *B*). Up to 65% of the sample has been classified as Sb or later. Near infrared data, stellar masses and the properties of the youngest stellar population were presented in Gil de Paz et al. (2000) and Pérez-González et al. (2003a).

This paper presents the narrow-band (*NB*) imaging in the redshifted $H\alpha$ passband for a subsample of 79 galaxies from the UCM Survey. The subset represents $\sim 40\%$ of the 191 galaxies within the Lists I and II of the survey. These galaxies were selected to ensure that all the spectroscopic types described in Gallego et al. (1996) were represented in the same proportion as in the parent sample. The representativeness of this subsample in $H\alpha$ equivalent width — $EW(H\alpha)$ — and luminosity has also been tested. A Kolmogorov-Smirnov test using $EW(H\alpha)$ (a good tracer of the spectroscopic type) for the subsample and the entire sample estimates the probability of the former being representative of the latter in 82%. The same test using the $H\alpha$ luminosity yielded a probability of 98%. Table 2 presents the sample along with the main results from this $H\alpha$ imaging study. For specific details on individual objects, the reader may refer to Pérez-González et al. (2003a) and references therein.

The 79 galaxies used in the present paper were observed in three different campaigns and two service nights at the Nordic Optical Telescope³ and two runs at the CAHA 2.2 metre telescope⁴. General information about the campaigns is provided in Table 1.

³The Nordic Optical Telescope is operated on the island of La Palma jointly by Denmark, Finland, Iceland, Norway, and Sweden, in the Spanish Observatorio del Roque de los Muchachos of the Instituto de Astrofísica de Canarias.

⁴German-Spanish Astronomical Centre, Calar Alto, operated by the Max-Planck-Institute for Astronomy, Heidelberg, jointly with the Spanish National Commission for Astronomy.

Table 1. Log for the H α observations.

Telesc./Observ. (1)	Date (2)	Instrument (3)	Scale (4)	Conditions (5)
NOT (service)	Jul 13 1999	HiRAC	0.110	photometric
2.2m CAHA	Dec 27–28 1999	CAFOS	0.313	cloudy
NOT	Sep 22–25 2000	ALFOSC ^a	0.189	1 photometric night
NOT (service)	Sep 16 2000	ALFOSC	0.189	photometric
2.2m CAHA	May 10–13 2001	CAFOS	0.313	non-photometric
NOT	Jun 22–26 2001	ALFOSC	0.189	photometric
NOT	Apr 19–21 2002	ALFOSC	0.189	2 photometric nights

^aThe data presented here have been taken using ALFOSC, which is owned by the Instituto de Astrofísica de Andalucía (IAA) and operated at the Nordic Optical Telescope under agreement between IAA and the NBIfAFG of the Astronomical Observatory of Copenhagen.

Note. — Observing log for the H α observations of the UCM Survey galaxies. Columns stand for: (1) Telescope name. (2) Date of the observation. (3) Instrument used (all equipped with a Loral 2k \times 2k detector). (4) Scale of the CCD in arcsec pixel⁻¹. (5) Weather conditions.

The observations included narrow-band imaging centered at the wavelength of the redshifted $H\alpha$ emission-line of each galaxy, and broad-band (Cousins- R_C) imaging. The broad-band data was used to subtract the continuum of the narrow band images. Typical exposure times were 900 seconds in R_C and 2700s in the NB , allowing us to reach a limiting surface brightness in $H\alpha$ (2σ) of $\sim 5 \times 10^{-17} \text{erg s}^{-1} \text{cm}^{-2} \text{arcsec}^{-2}$. The total exposure was split in several sub-exposures for cosmic ray and artifact elimination. About 90% of the frames were taken in subarcsecond seeing conditions.

Some of the data reduction and measurements were carried out using several IRAF tasks⁵, mainly *ccdproc*, *imcombine* and *geomap*. Other procedures were specially built for this work, including the fringing correction, continuum subtraction, and flux measurement programs. Standard steps were followed in bias subtracting and flat-fielding. Some of the broad band data presented a small level of fringing (1 count per 1000), which was eliminated using an object-free pattern built as a combination of all the frames taken during each night. Scaling of the pattern was performed for each image. After reduction, the images were aligned using the positions of ~ 10 stars, and all the frames of the same galaxy obtained with the same filter were combined.

Emission-line images were obtained by subtracting the continuum. This was achieved through the comparison of at least 20 field stars per frame whose emission-line fluxes were forced to be null in the final frames. Based on the standard deviation of the ratios between the fluxes of the stars in the NB and the broad-band images, we estimate a $\sim 5\%$ error in the subtraction of the continuum. The procedure left a residual sky background in the $H\alpha$ images, which was subsequently subtracted.

Landolt (1992) stars were observed in order to calibrate the R_C frames. We included a $B - R_C$ colour term in the calibration. $B - r$ colours were taken from Pérez-González et al. (2000) and converted to $B - R_C$ using a mean value of $r - R_C = 0.36$ (Fukugita et al. 1995). This colour is expected to vary in less than 0.04 magnitudes from one morphological type to another. Standard spectrophotometric stars (Oke 1990; Hamuy et al. 1992) were also observed to check the values of the scale factor between the R_C and NB filters. Images taken during non-photometric nights were calibrated with short R_C exposures obtained in other campaigns during photometric conditions.

In addition, 8 frames without photometric observations were calibrated using the Gunn- r data given in Vitores et al. (1996a). In order to do that, we first determined the correlation

⁵IRAF is distributed by the National Optical Astronomy Observatories, which is operated by the Association of Universities for Research in Astronomy, Inc. (AURA) under cooperative agreement with the National Science Foundation.

between the $R_C - r$ and $B - r$ colours in $5''$ apertures with the data of the galaxies observed in photometric conditions, obtaining $R_C - r = (-0.238 \pm 0.038) + (0.011 \pm 0.047)(B - r)$. The unbiased standard deviation of the correlation is 0.08^m . This relationship was then used to calculate the R_C magnitudes and to calibrate the frames obtained in non-photometric conditions. In order to estimate the magnitude of the calibration uncertainties, 2–3 common objects were observed in all the campaigns.

The transmission curves for all the NB filters used (and also R_C) were obtained from the observatories. Typical widths for the NB filters were 50 \AA . This value is not small enough to completely avoid contamination from the $[\text{N II}]\lambda 6548$ and $[\text{N II}]\lambda 6584$ lines. However, the transmissions at these wavelengths were often rather low in comparison with that of the $\text{H}\alpha$ line (1/2 on average). Pure $\text{H}\alpha$ fluxes were obtained taking into account these filter transmissions for the three lines, the $[\text{N II}]/\text{H}\alpha$ ratios given by Gallego et al. (1996) for each object, and the scale factors between the R_C and NB images obtained with field stars. To estimate the extinction corrections, the spectroscopic $\text{H}\alpha/\text{H}\beta$ ratios in Gallego et al. (1996) were used. These ratios were corrected for a stellar absorption of 3 \AA (Trager et al. 1998; González Delgado et al. 1999) and converted to $E(B - V)$ using the Galactic extinction curve of Cardelli et al. (1989).

We show $\text{H}\alpha$ and Cousins- R_C images of some example galaxies in Figure 1.

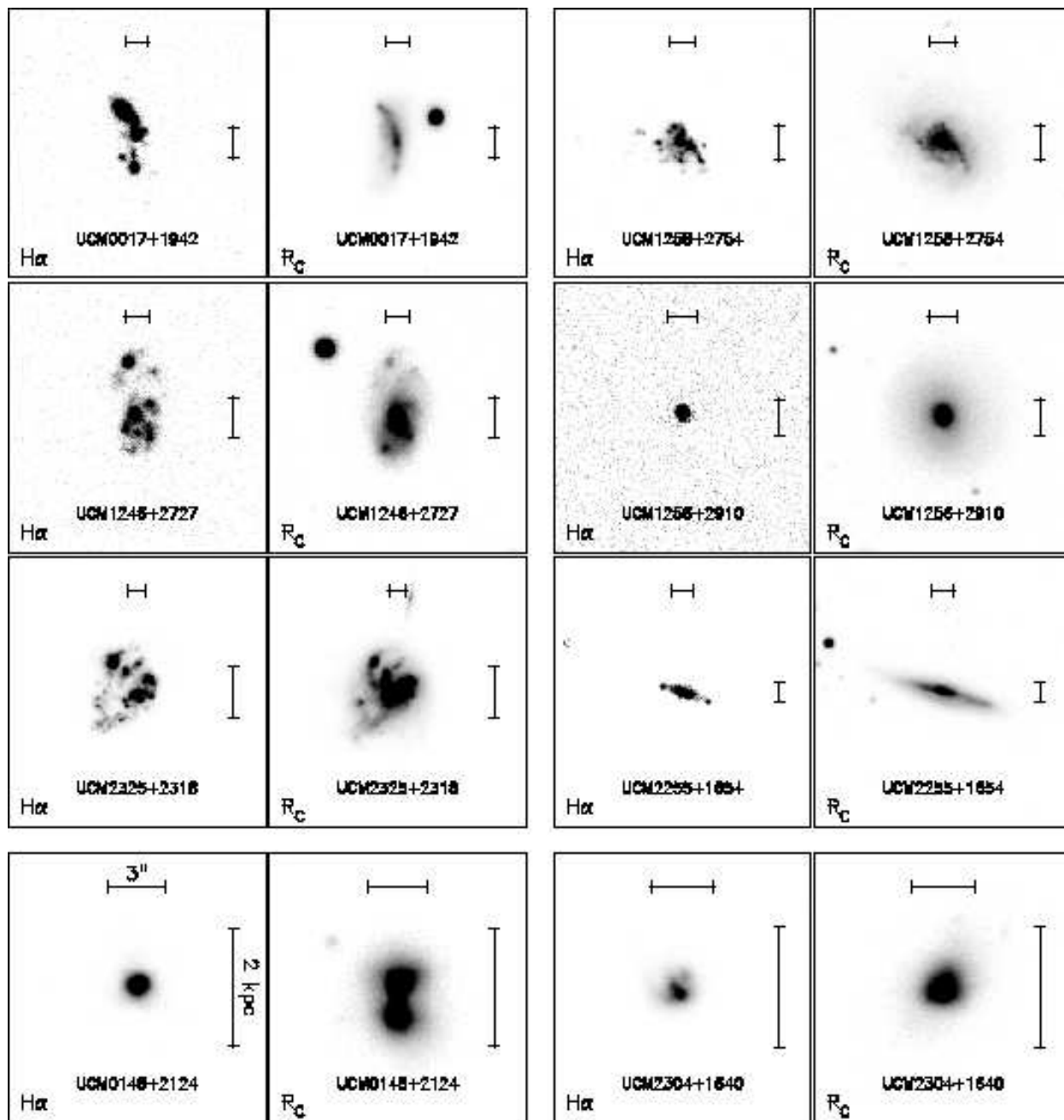


Fig. 1.— Gray-scale representation of some of the images of the UCM Survey galaxies. For each object, H α and Cousins- R_C images are shown. North is up and east is left. An angular size of 3'' is marked at the top of each image (horizontal segment). A 2 kpc transversal distance is also depicted on the right of each image (vertical segment). The 3 first rows plot HII-*like* galaxies (on the left) and disk-*like* objects (right). The 2 objects in the last row are BCDs. The images for the entire sample can be accessed in http://www.ucm.es/info/Astrof/UCM_Survey/UCM/ha_images.html.

3. Results

3.1. Spectra vs. imaging

One of the main goals of the present work was to determine the amount of $H\alpha$ emission falling outside the slit employed in the spectroscopic follow-up of Gallego et al. (1996). The issue becomes very important when spectroscopic data are used to characterize extended objects. Different approaches have been followed when facing the problem, ranging from aperture corrections based in broad-band fluxes (Gallego et al. 1995) to the absence of any correction (Kauffmann et al. 2002).

First, we compared spectroscopic and imaging observations by simulating the long-slit in the $H\alpha$ frames. Artificial slits were simulated using the information about position angles and widths given by Gallego (1995). The centers were chosen as the intensity peaks in the broad-band images, similarly to what was done in the spectroscopic campaigns. The measurements were repeated 8–10 times with small random variations of the center position and angle, and then averaged to obtain the most probable value. The average values of the spectroscopic fluxes and those measured from the simulated slits are identical (the average difference is lower than 1%), although the median fluxes are 5% larger in the case of the simulated slits. This is probably related to the fact that the simulated apertures were more extended along the slit than those used by Gallego et al. (1995). Still, individual differences are reasonably below typical spectroscopic uncertainties.

The integrated $H\alpha$ flux for each object was measured using polygonal apertures enclosing the entire galaxy and also a curve of growth built with circular apertures. The estimated errors include Poisson statistics, uncertainties in the sky determination, the standard deviation of the photometric zero-points, and the errors associated with the continuum subtraction.

Figure 2 shows the comparison between the $H\alpha$ fluxes measured in the spectra and the total $H\alpha$ emission in the images (decontaminated from $[N II]$ emission). Symbol sizes are related to the effective radii in the B -band (in arcsec). On average, the spectroscopic follow-up of the UCM Survey galaxies detected one third (1/3.0) of the total emission-line flux due to the finite width or a improper positioning of the slit. Due to the asymmetry in the distribution, the corresponding median factor is one half (1/2.0). As expected, the agreement between photometric and spectroscopic fluxes is better among the compact objects.

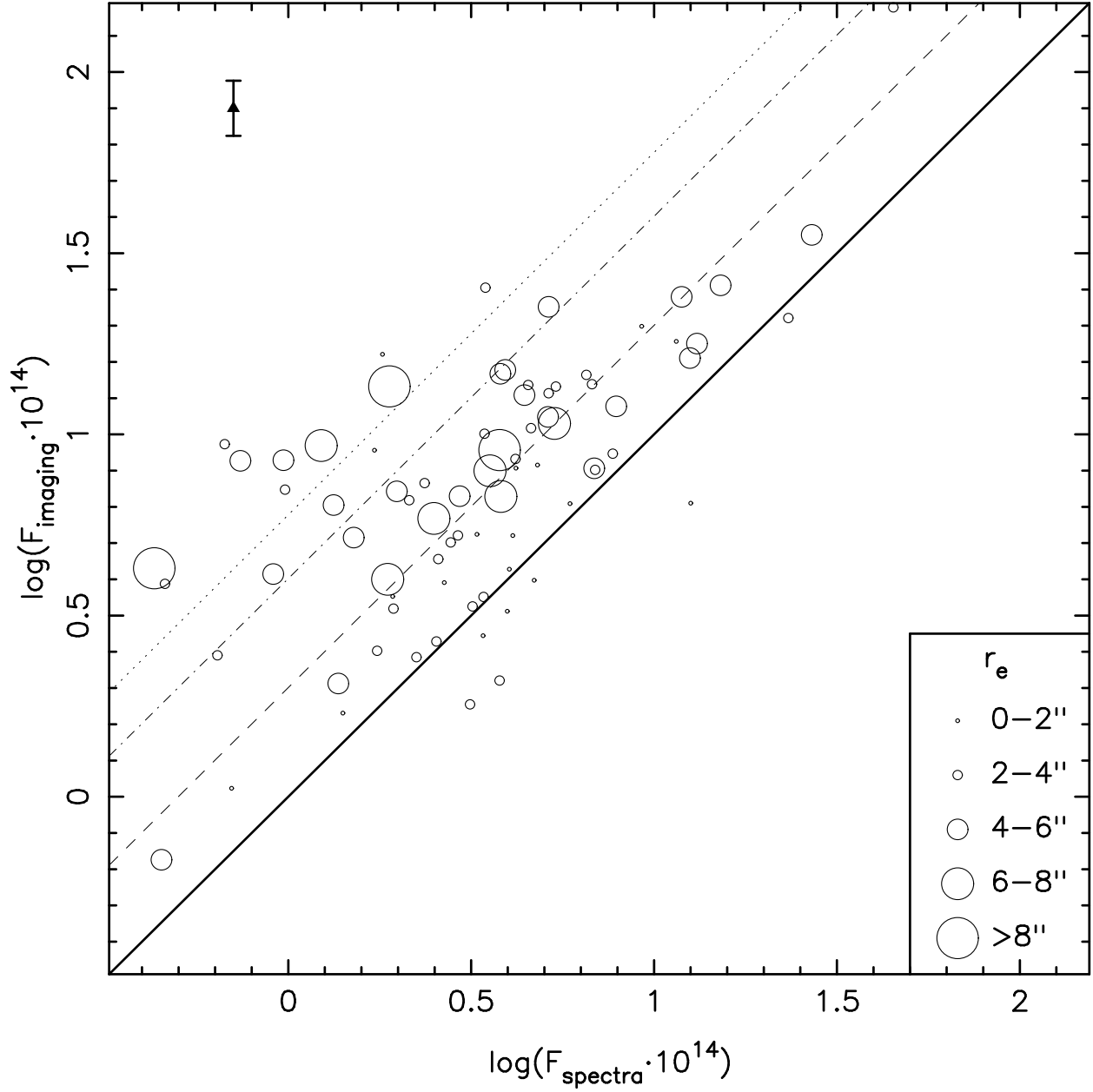


Fig. 2.— Comparison of the H α fluxes determined for the spectroscopy and those obtained from the integrated emission measured in the images (in $\text{erg s}^{-1} \text{cm}^{-2}$). Symbol sizes are related to the effective radii in the B-band (see legend). The lines correspond to $F_{\text{imaging}}/F_{\text{spectra}}$ ratios of 1, 2, 4 and 6. The average error in the H α fluxes derived from the images is shown.

Our data also indicates that the global $EW(H\alpha)$ values determined from the imaging data are, on average, a factor 1.8 ± 1.2 smaller than the ones obtained with the long-slit spectroscopy. This value is independent of the galaxies' spectroscopic type. Similar differences have been observed in normal spirals (Kennicutt & Kent 1983). This can be understood because the $EW(H\alpha)$ is related to the ratio of newly-born stars (responsible for the emission lines) to the evolved underlying population, and thus we expect this quantity to be large for galaxies with relatively important bursts of recent star formation, specially at very young ages. Since the spectroscopic observations tend to concentrate on the brightest star-forming knots, it is not surprising that the $EW(H\alpha)$'s derived from the spectra are higher than the galaxies' global values. In addition, the UCM sample is dominated by objects with bright nuclear starbursts (Gallego et al. 1996), and again we expect the $EW(H\alpha)$ measured for the entire galaxy to be smaller than the spectroscopic values. The exception to this are the galaxies for which the long-slit was placed in the galaxy center and missed bright HII regions in the disk.

3.2. Concentration and size properties

The UCM Survey galaxies present enhanced star formation when compared with 'normal' quiescent spiral (or lenticular) galaxies (Gil de Paz et al. 2000; Pérez-González et al. 2003b). Several triggering mechanisms are usually postulated for the activation of massive star formation: tidal forces, mergers, supernova winds, etc. These processes are more efficient in the central nuclear zones of the galaxies, where the potential well is deeper and higher gas densities are found (see Kennicutt 1998a, Combes 2001, and references therein). Gas stability criteria would also favour violent star formation events at low radial distances (Quirk 1972; Kennicutt 1989). Therefore, it is not surprising that 57% of the entire UCM sample was spectroscopically classified as *starburst nuclei* galaxies. These objects are supposed to be experiencing a massive burst characterized by a high metallicity and low excitation (Gallego et al. 1996) and placed in the inner parts of the galaxy. Another 32% of the entire survey are *HII-like* galaxies presenting low metallicities and high excitations. Their star formation could be more extended and/or not linked with the galactic nucleus.

In this section and the next one, we will study the location of the starburst knots. First, we will focus on the concentration properties of the current star formation in the UCM Survey galaxies. We have calculated the concentration index c_{31} for the $H\alpha$ emission. This index was defined by Gavazzi et al. (1990) as the ratio between the radii of the aperture containing 75% and 25% of the total flux. We have used isophotal apertures centered in the maximum of the broad-band images. Figure 3 shows the distribution of c_{31} for our

sample of galaxies. The median value and quartiles for the entire sample are indicated. A wide range of concentrations are observed. The peak of the distribution is found at $c_{31} = 2\text{--}3$, corresponding to galaxies with extended star formation. These values are typical of disk-dominated objects when the morphological classification is based on broad-band concentration indices (Gavazzi et al. 1990; Vitores et al. 1996b; Pérez-González et al. 2001). Our sample also includes rather concentrated galaxies with values of c_{31} up to 10.

We must be cautious when interpreting the concentration indices obtained in $H\alpha$ images and their possible links with nuclear and disk star formation. High concentrations may be found in galaxies with no nucleus or bulge at all but presenting one very bright and intense burst (e.g, BCDs). In contrast, a single nuclear burst occupying all the bulge with a flat surface brightness profile may present a rather low c_{31} value. A more appropriate parameter for the discussion on nuclear and disk emissions will be used in Section 3.3.

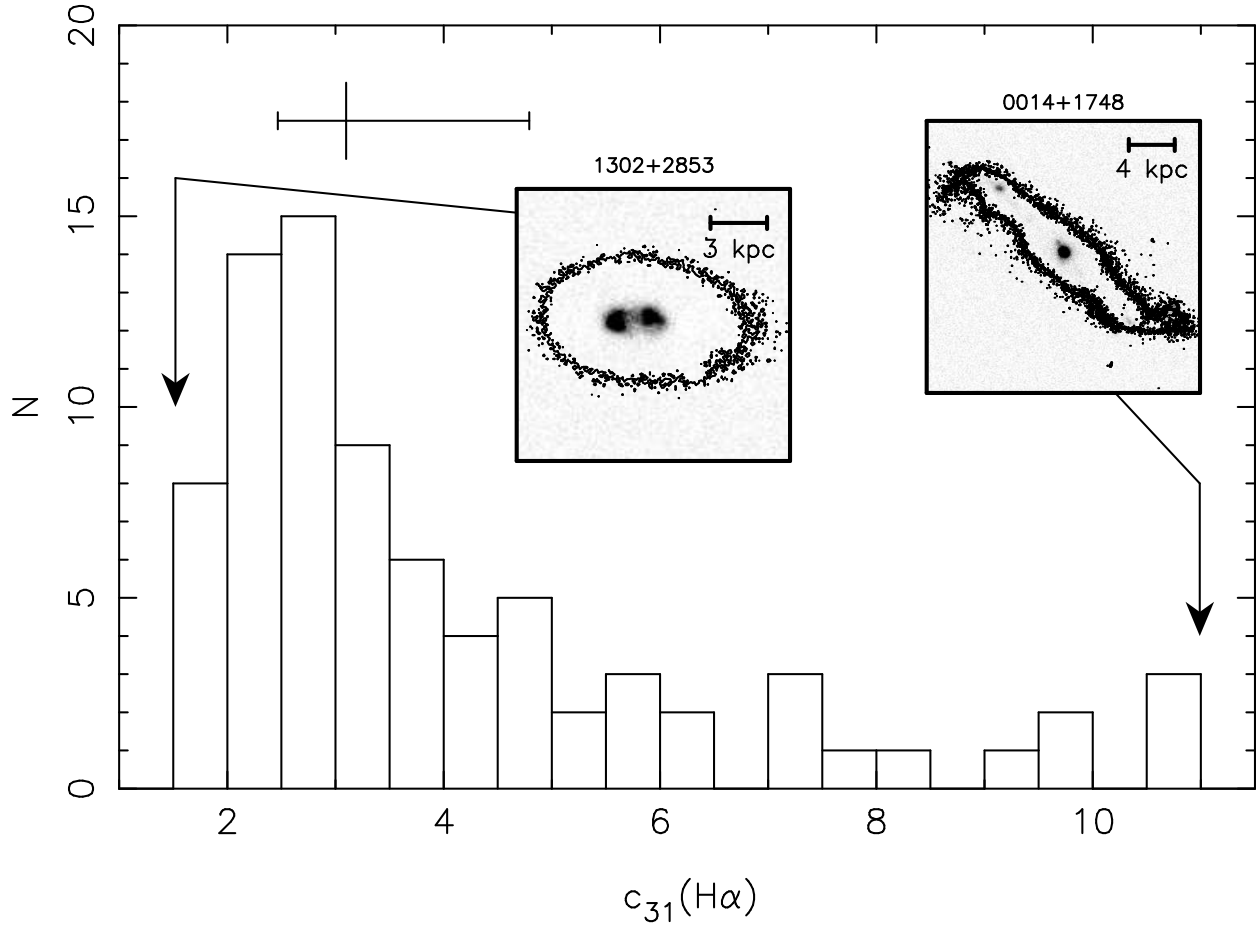


Fig. 3.— Distribution of the c_{31} concentration index for the UCM sample. The median value and quartiles are shown by the error bar. The $\text{H}\alpha$ images for two extreme cases are plotted in gray-scale. Overimposed on them are the contour for the pixels with a surface brightness of $23.5 \text{ mag arcsec}^{-2}$ in the R_C image. North is up and east is left.

Another important point to consider when studying the concentration of the emission is the size of the starburst zone. In Figure 4 we have plotted the histogram of the effective radius (i.e., radius containing half of the light) of the $H\alpha$ emission. The distribution peaks at ~ 1 kpc, with three quarter of the galaxies presenting effective radii smaller than 3 kpc. The median value is almost identical (ours is 0.02dex larger) to that found by Lehnert & Heckman (1996) for a sample of edge-on, infrared-warm, starburst galaxies, and $\sim 15\%$ larger than the values given by Chitre & Joshi (2001) for a sample of Markarian galaxies. The distribution of effective radii in the R_C -band is also presented in this figure. The average is ~ 2.5 kpc, which is also in complete agreement with Lehnert & Heckman (1996). Although we also find a size-luminosity relationship as the one claimed by these authors, the scatter is very large. The Spearman’s rank-order correlation coefficient is 0.51 and the two-sided significance level of its deviation from zero is 2×10^{-6} . These size distributions reveal that, in a significant fraction of the UCM galaxies, the star formation tends to be more concentrated than the older underlying stellar population.

We also find a tendency for galaxies with late-type morphologies to have larger $H\alpha$ effective radii. The median values are: 0.51 kpc for S0, 0.82 kpc for Sa, 1.38 kpc for Sb, 1.91 kpc for Sc+ and 2.12 kpc for irregulars. The median for the sample of BCDs is 0.53 kpc. The segregation is also noticeable in the case of spectroscopic types: *disk-like* galaxies present larger values (1.51 kpc) than *HII-like* objects (0.62 kpc).

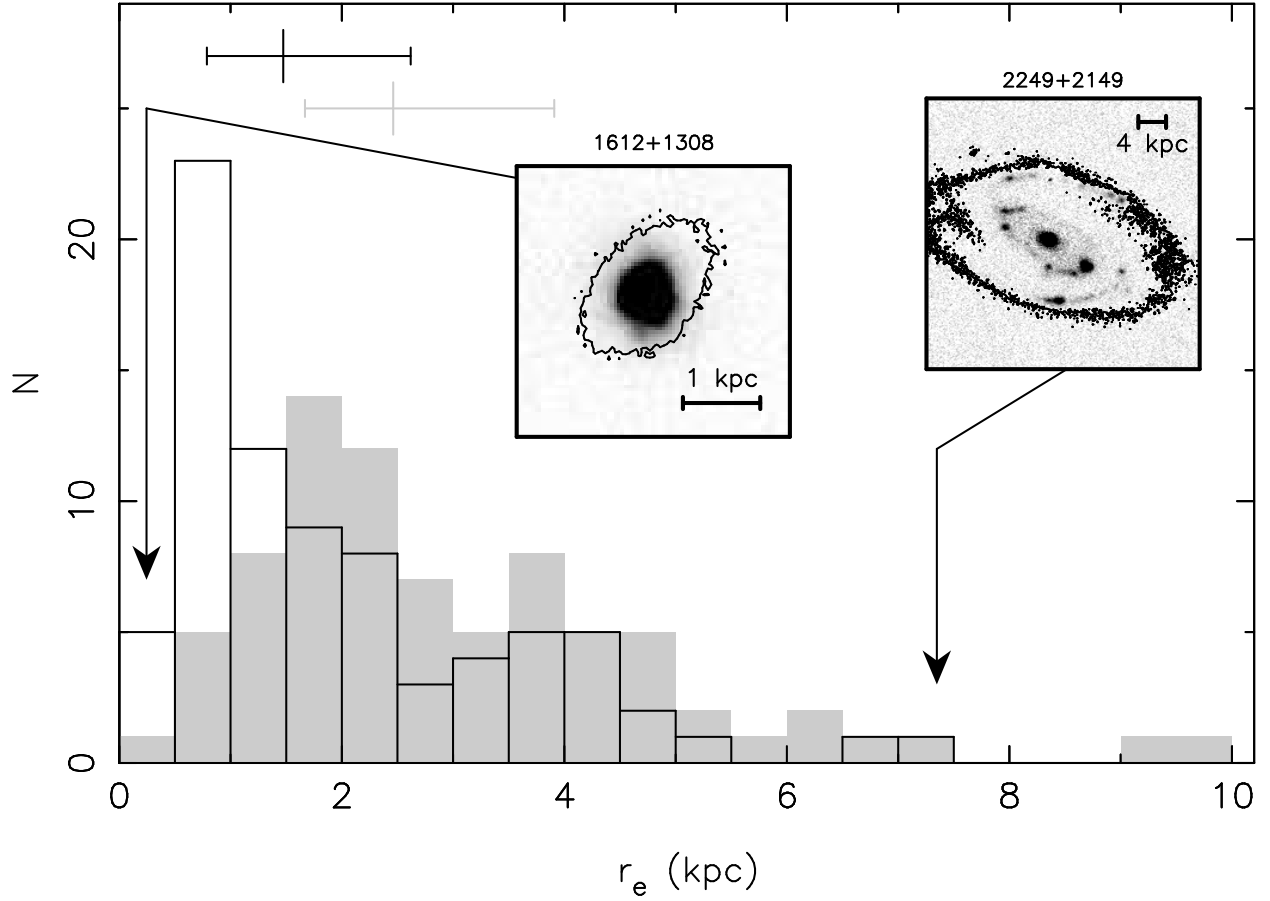


Fig. 4.— Distribution of the effective radii (in kpc) of the H α (solid-line) and continuum R_C (gray histogram) emission of the UCM Survey galaxies. As before, the H α images for two extreme cases are shown (cf. figure 3).

Figure 5 presents the histogram of the ratios of the sizes of the emitting regions and the host galaxies. As a measurement of the size of the star formation zone we use the radius of the circular region containing 80% of the total H α emission. The total size of the galaxy has been taken as the radius of the 24.5 mag arcsec⁻² isophote in the R_C image. Both regions have been centered on the maximum-intensity pixel of the broad-band image. As a consequence, the ratio between the sizes of the H α and continuum emissions is strongly affected by the anisotropy of the star formation along the galaxy. In particular, this parameter is strongly affected by the existence of bursts in the outer parts of the object. The median value of the ratio is 0.5, i.e., the radius of the region where there is active star formation is half of the total optical radius of the galaxy. The values spread from objects where even the most external zones of the galaxy are involved in the burst process (e.g., UCM1303+2908 and UCM1444+2923) to very concentrated galaxies (e.g., UCM0159+2328 and UCM1256+2910). The former are associated with late-type spirals and irregulars (median values range from 0.5 for S0/Sa to 0.8 for Sc+/Irr, BCDs and interacting systems). No major differences are found between the average values of disk and HII-*like* galaxies.

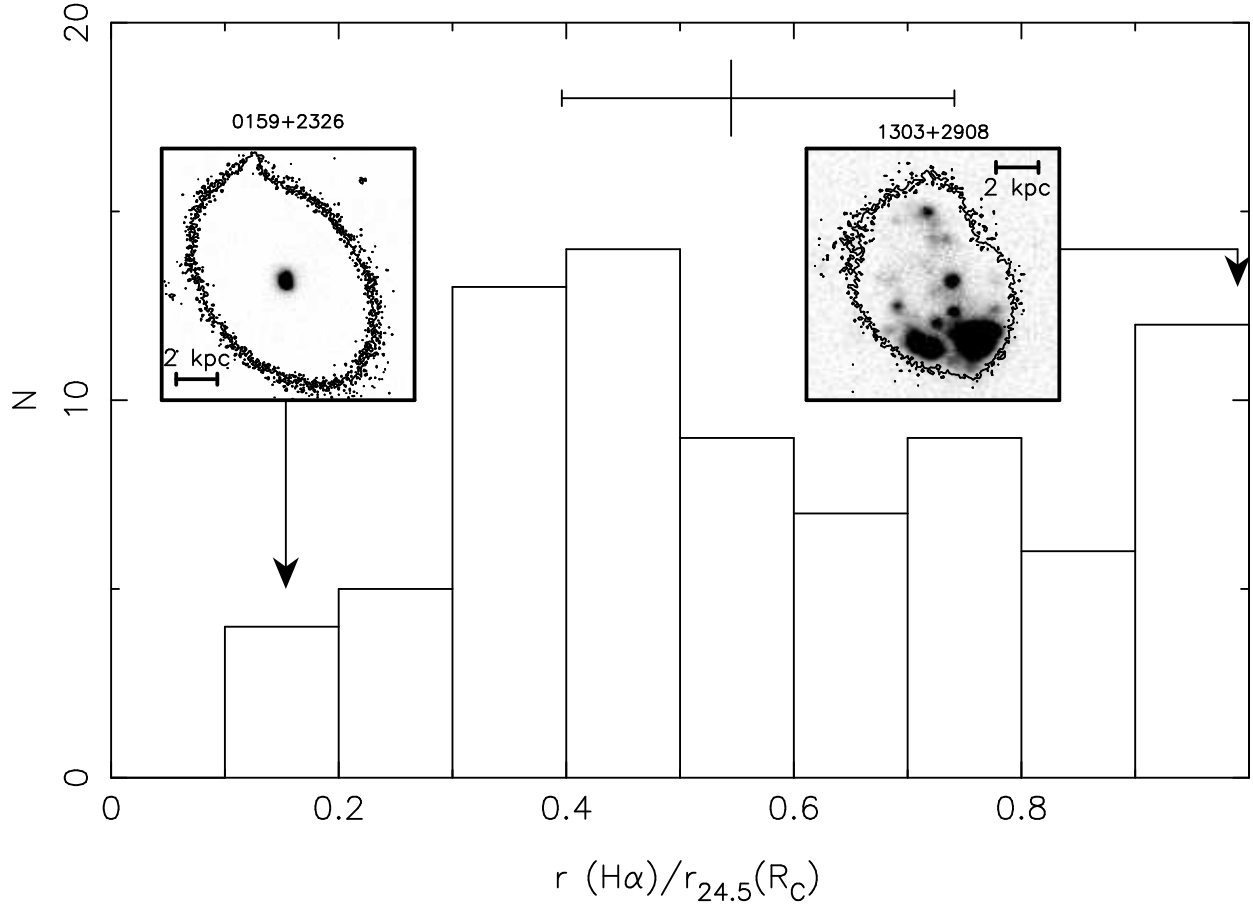


Fig. 5.— Histogram of the ratio between the sizes of the $\text{H}\alpha$ emitting region (the radius of the circular region containing 80% of the total $\text{H}\alpha$ emission) and the entire galaxy (radius of the 24.5 mag arcsec^{-2} isophote in the R_C image).

The relative sizes of the star-forming region and the host galaxy may also be studied by comparing the area of the H α emitting zone and the total extension of the object. This parameter is not affected by the anisotropy of the star formation. The area of the burst has been calculated using the procedure explained in Section 3.5, and the extension of the galaxy has been assumed to be the area inside the 24.5 mag arcsec⁻² isophote. The distribution for the entire sample is flat, with a median value of 0.5 and quartiles at 0.3 and 0.9. Again, a correlation with Hubble type is observed (from 0.3 for S0/Sa to 0.7 for Sc+/Irr and 1.0 for BCDs). On average, disk-*like* galaxies harbor a star-forming event covering $\sim 40\%$ of the area of the galaxy, while $\sim 70\%$ of the area is covered by star formation in the case of HII-*like* objects.

Our study of the sizes of the star-forming regions in local galaxies is of direct relevance to the interpretation of spectroscopic data from large galaxy surveys such as the Two Micron All Sky Survey (2MASS, Jarrett et al. 2000) or the Sloan Digital Sky Survey (SDSS, Stoughton et al. 2002). In these surveys, the spectroscopic data is obtained using multi-object spectrographs which utilize multi-slit masks or fibers. These slits and fibers have a finite size and force to consider aperture corrections. Our imaging study may be used to estimate the importance of these corrections. For example, Figure 6 shows the distribution of the ratios of the H α flux within an aperture of 3'' (used by the SDSS) to the total H α flux. A large spread exists in the fractional coverage of the UCM galaxies by this aperture size. The median of the distribution reveals that the SDSS fibers would miss typically 40% of the total H α emission of UCM-like galaxies, and that more than half of the flux would be missed for 40% of our sample.

The inset in the top-left corner of Figure 6 shows the change with redshift of the observed-to-total H α flux ratio in a 3'' circular aperture. We have artificially redshifted the UCM galaxies from their measured redshifts up to $z = 1$ in $\Delta z = 0.01$ steps, and estimated the fraction of the fluxes that would be detected inside a 3'' spectroscopic fiber (or slit) for each redshifted object. The calculated points in the top-left panel of Figure 6 are the averages for the entire sample. They have been fitted with a polynomial curve. This plot reveals that only beyond redshift ~ 0.1 the 3'' aperture contains more than 95% of the total flux. For redshifts below this limit, corrections to the H α aperture fluxes are non-negligible.

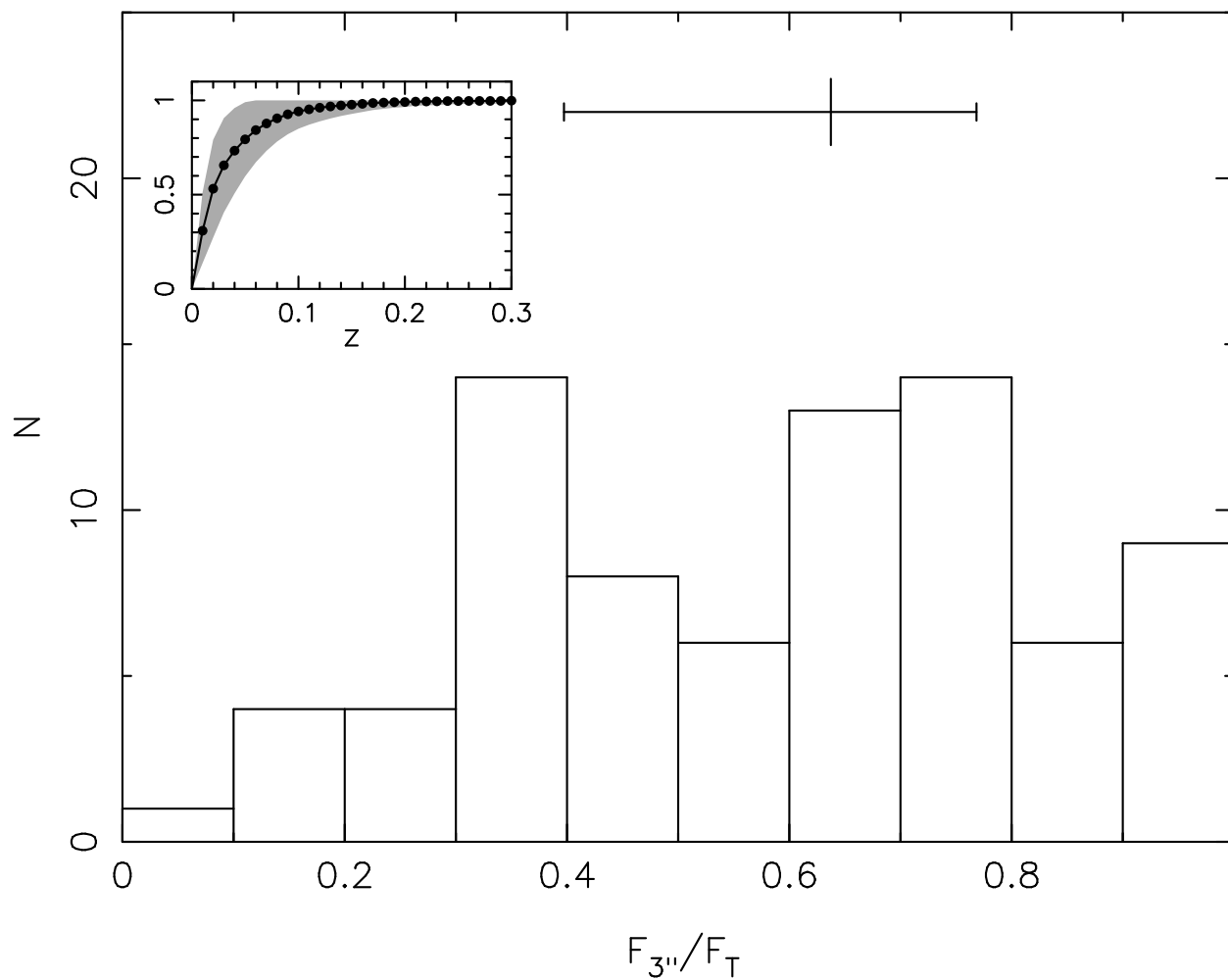


Fig. 6.— Comparison of the H α emission within a circular aperture of 3'' (typical of wide field and all sky surveys such as 2MASS or SDSS) to the total flux for the UCM galaxies. The inset in the top-left corner shows the change with redshift of the flux ratio in a 3'' circular aperture. The values for the entire sample have been calculated by artificially-redshifting the UCM galaxies. Mean values, standard deviations (shaded area) and a polynomial fit are shown.

3.3. Nuclear vs. disk emission

The relative contribution of the nuclear and the disk components to the total H α luminosity will be studied in this section. As we mentioned in Section 3.2, concentration indices may lead to errors when analyzing the location of the starbursts if a bulge-disk characterization is not performed previously. Bulge-disk decomposition for the UCM Survey galaxies was carried out in the Gunn- r and Johnson- B bands by Vitores et al. (1996b) and Pérez-González et al. (2001), respectively. Using the results for the red filter, we have considered:

$$F_T^\alpha = F_{\text{bulge}}^\alpha + F_{\text{disk}}^\alpha = \frac{\int_0^\infty F^\alpha(r) \cdot I^r(r) \cdot r \cdot dr}{\int_0^\infty I^r(r) \cdot r \cdot dr} \quad (1)$$

where F_T^α is the total H α flux, $F^\alpha(r)$ is the radial dependent H α flux, $I^r(r) = I_{\text{bulge}}^r + I_{\text{disk}}^r$ is the intensity in the Gunn- r filter, and the integral extends over all radii.

Identifying the nuclear component with the bulge, the H α flux F_{bulge}^α arising from this area can be calculated using:

$$F_{\text{bulge}}^\alpha = \frac{2\pi}{L_T^r} \cdot \int_0^\infty F^\alpha(r) \cdot I_{\text{bulge}}^r(r) \cdot r \cdot dr \quad (2)$$

where L_T^r is the integrated luminosity in the r filter. An analogous expression can be built for the H α flux of the disk. In Vitores et al. (1996a), the bulge intensity profile was fitted using a de Vaucouleurs (1948) exponential function, and the disk intensity was fitted by a Freeman (1970) law. In order to calculate the numerator of Equation 2, the function $F^\alpha(r)$ was approximated by a series of Chebyshev polynomials. The integral was calculated using a Gauss-Laguerre quadrature.

The method described above was used to obtain the ratio between the bulge and the total H α luminosities $-(B/T)(H\alpha)-$. The goodness of the bulge-disk decompositions was checked interactively for each individual object.

The median and standard deviation of the $(B/T)(H\alpha)$ ratios of the sample are 0.26 ± 0.26 . This means that a typical UCM galaxy harbours a star formation event with $\sim 30\%$ of nuclear component. Therefore, whereas the spectroscopic classification was mainly dominated by starburst nuclei (SBN, Balzano 1983) galaxies, the images reveal that simultaneously to the nuclear burst there exists an important amount of recent star formation occurring in the disk. A segregation of $(B/T)(H\alpha)$ values according to the spectroscopic classification has been observed: *disk-like* objects present a median of 0.33 ± 0.26 and *HII-like* 0.15 ± 0.26 . The $(B/T)(H\alpha)$ is correlated with morphological type in the UCM Survey, as some authors

have claimed for other samples (see, e.g., Kennicutt 1983, 1998a; Lehnert & Heckman 1996). The median values are: 0.43 for lenticulars, 0.45 for Sa, 0.36 for Sb, and 0.05 for late Hubble types (Sc+/Irr) and BCDs.

3.4. Equivalent width and luminosity

In Section 3.1, we argued that $EW(H\alpha)$ provides a measurement of the relative importance of newly-formed stars with respect to the older population. Unlike ‘normal’ spiral galaxy samples, all the spiral galaxies in the UCM sample have median integrated $EW(H\alpha)$ (based on imaging data) of about 40 – 50 Å. Even more intense star formation is found in irregulars (the average is 70 Å), BCDs (110 Å), and interacting systems (60 Å). The correlation observed between morphological type and $EW(H\alpha)$ for normal galaxies (Kennicutt & Kent 1983; Sauvage & Thuan 1994; Gavazzi et al. 1998) is not present in our sample, probably as a consequence of the enhanced star-forming activity of the UCM galaxies (see Section 3, and figure 1 in Pérez-González et al. 2003a). This is directly related to selection effects of the survey, biased towards the detection of objects with high $EW(H\alpha)$ (larger than ~ 20 Å, Gallego 1995).

Spectroscopically, *disk-like* galaxies present considerable lower values of the $EW(H\alpha)$ (24 Å) than *HII-like* objects (75 Å). This is directly related to the findings of Gil de Paz et al. (2000) and Pérez-González et al. (2003b): *HII-like* objects have higher SFR per unit stellar mass than *disk-like* galaxies.

The integrated $H\alpha$ emission has been found to be strongly correlated with optical colours (Kennicutt & Kent 1983; Kennicutt et al. 1984; Davidge 1992). This means that the youngest stars, though not contributing much to the total stellar mass of the galaxy ($\sim 5\%$ for the UCM galaxies, cf. Pérez-González et al. 2003b), have a major influence on the integrated optical colours. The correlation is also observed for the UCM sample and is plotted in Figure 7. The large scatter of this plot is related to differences in star formation history and dust extinction.

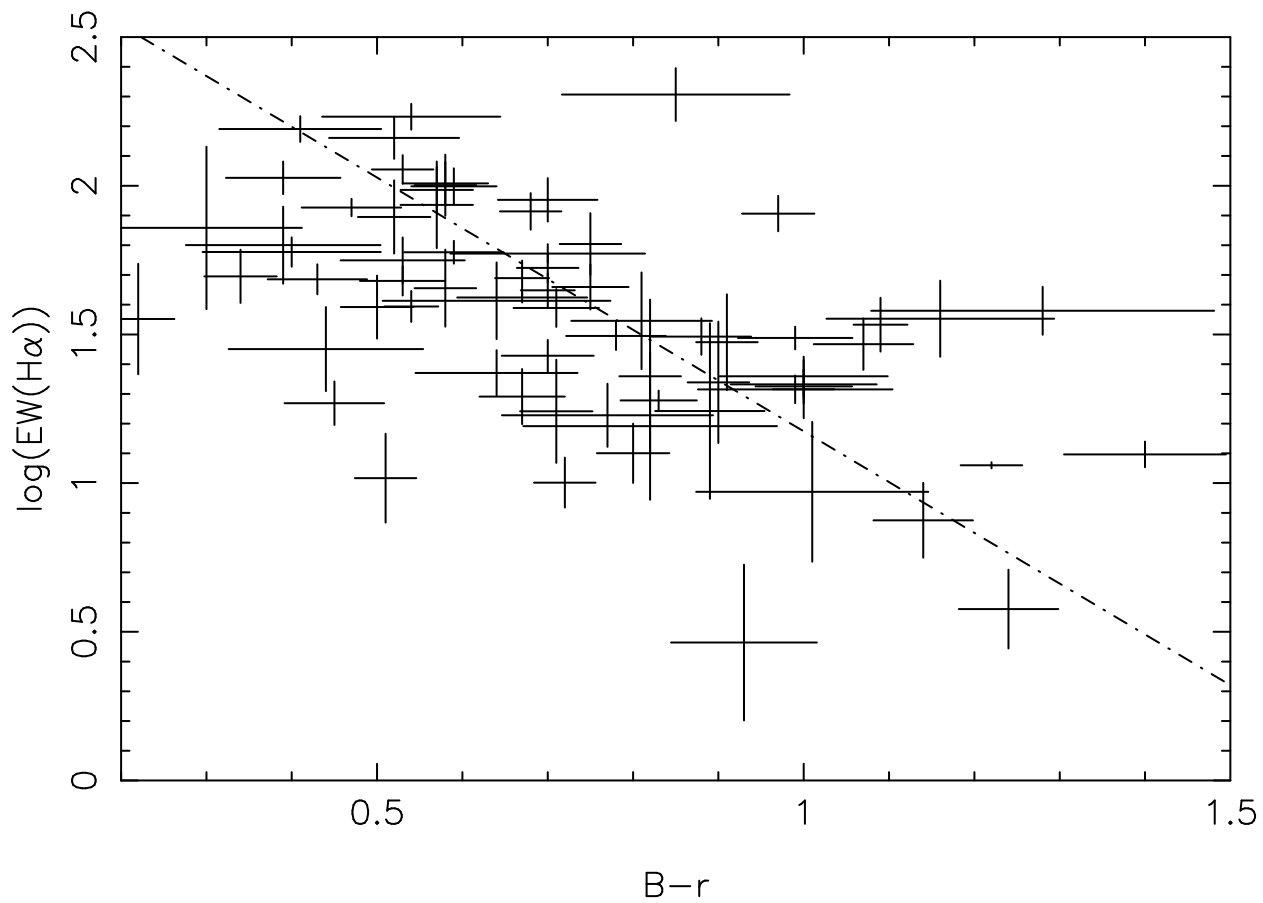


Fig. 7.— Integrated optical colour ($B - r$) vs. imaging equivalent width (\AA) relationship. The best fit is plotted: $\log(EW(H\alpha)) = (-1.707 \pm 0.091) \times (B - r) + (2.881 \pm 0.066)$. The Spearman’s rank-order correlation coefficient is -0.55 and the two-sided significance level of its deviation from 0 is 4×10^{-7} .

As the next step in our study, we have calculated the $H\alpha$ luminosities for the entire sample so that we can compare the imaging-based results with those obtained from spectroscopy (cf. Section 3.6). But before we carry out such comparison, it is interesting to see whether the measured luminosities (or the derived SFRs) correlate with any other observables. In Figure 8 we have plotted the SFR against the $H\alpha/H\beta$ ratio, a useful extinction estimator. SFRs have been calculated using the conversion factor given in Sullivan et al. (2001), almost identical to the one obtained by Kennicutt (1998a):

$$SFR = \frac{L(H\alpha)(erg\ s^{-1})}{1.22 \times 10^{41}} \mathcal{M}_{\odot}\ yr^{-1} \quad (3)$$

Figure 8 shows a clear correlation between the derived SFRs and the extinction. Objects with larger obscurations have also larger SFRs. This effect was also noticed in the stellar population synthesis analysis presented in Pérez-González et al. (2003b), where not only high-extincted galaxies showed higher burst strengths (ratio between the mass of newly-formed stars and the total stellar mass), but they also seemed to follow different extinction laws than low-extinction objects.

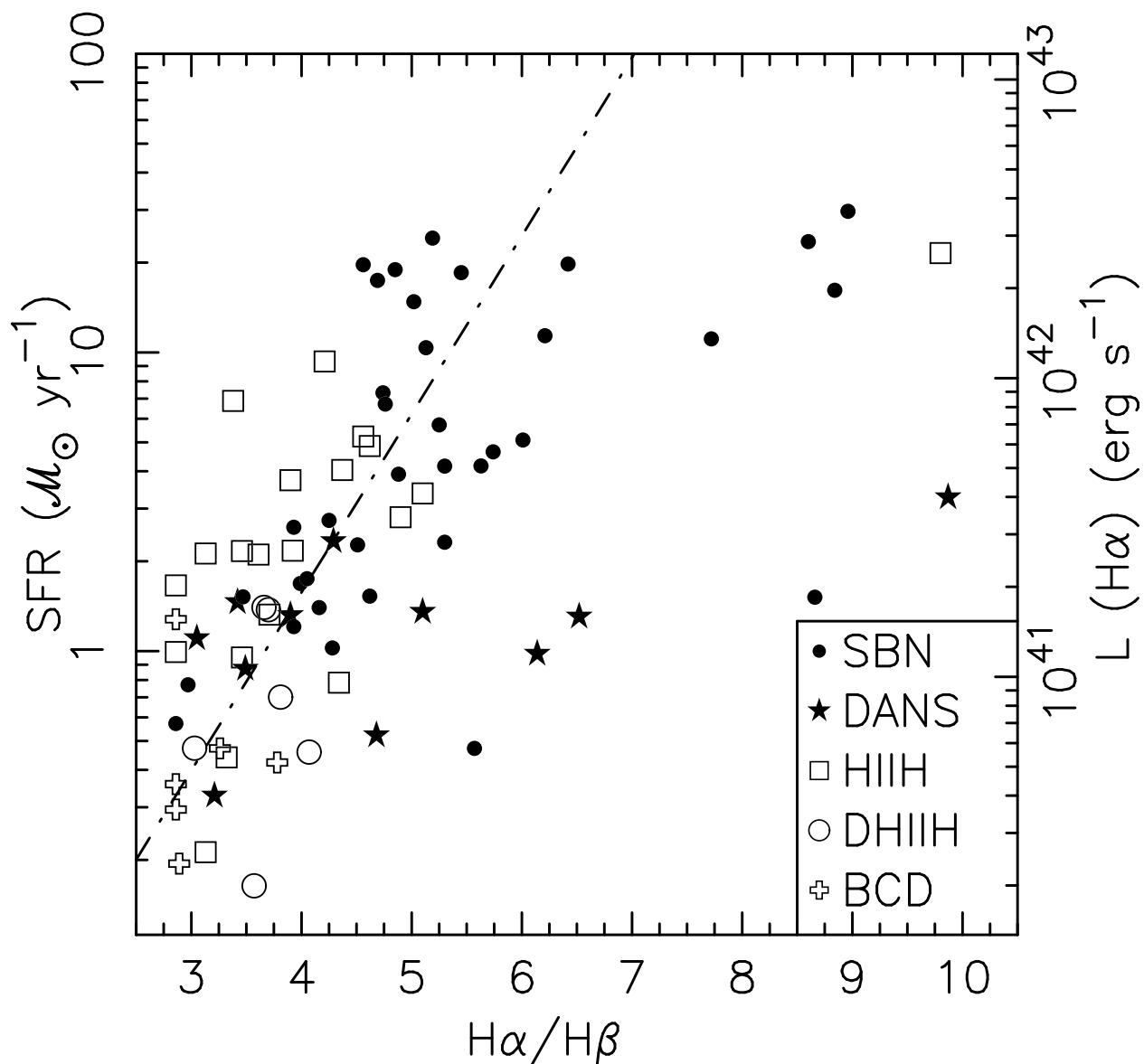


Fig. 8.— Relationship between extinction and SFR (or $H\alpha$ luminosity, as shown on the right-hand side axis). The best linear fit to the data, which takes into account observational errors, is shown (see text). Different symbols are used for different spectroscopic types (see legend). Filled symbols correspond to disk-like galaxies and open ones to HII-like objects (see Gallego et al. 1996, and Section 2).

The correlation between SFR and extinction has also been reported in previous works (e.g., Hopkins et al. 2001; Sullivan et al. 2001). Our fit to the relationship between the SFR and the Balmer decrement (corrected by stellar absorption) is, taking into account observational errors:

$$\log(SFR) = (0.597 \pm 0.021) \times \frac{H\alpha}{H\beta} + (-2.191 \pm 0.086) \quad (4)$$

The Spearman’s rank-order correlation coefficient is 0.67 and the two-sided significance level of its deviation from 0 is 2×10^{-11} . The derived slope is much larger than the one given in Sullivan et al. (2001) and Hopkins et al. (2001). It is interesting to notice that the correlation seems to saturate for very reddened objects ($H\alpha/H\beta \gtrsim 7$, corresponding to $E(B - V) \gtrsim 0.9$), and therefore the derived regression is not valid for very high extinction values. This behaviour was not observed by Sullivan et al. (2001) since their ultraviolet-selected nearby galaxy sample lacks very highly-obscured objects. This is not surprising: the selection at ultraviolet (UV) wavelengths is strongly biased against highly obscured objects. Note also that if we only consider the objects in our sample with Balmer decrements lower than 5.5 (i.e., low-to-moderate extinction), the correlation we find becomes very similar to the one found by Sullivan et al. (2001).

Most of the objects which do not follow our observed correlation are *disk-like* galaxies. Note also that the DANS (Dwarf amorphous nucleated spheroidals, Salzer et al. 1989) seem to follow a different relation from the rest of the objects, presenting relatively low and almost constant SFRs ($\sim 1 \mathcal{M}_{\odot} \text{ yr}^{-1}$) for all obscurations. This spectroscopic class, the low luminosity version of SBN objects, has already shown significant differences in other properties such as their stellar mass and SFR per stellar mass (Pérez-González et al. 2003b).

The breakdown of the SFR–extinction relationship at high $H\alpha/H\beta$ could be a symptom of the fact that, at large obscurations, extinction indicators such as the Balmer decrement or the slope of the UV continuum fail to correct the observed luminosities (Bell 2002). This is also supported by observations of some ultraluminous infrared galaxies, where the UV slope indicates a lower extinction than that derived from the UV to far infrared (FIR) ratio (Goldader et al. 2002). Observations of the UCM sample in the FIR would be necessary to ascertain whether, by using the observed $H\alpha/H\beta$, we significantly underestimate the extinction (and thus the SFR) in some heavily-obscured star-forming regions within the galaxies. It could well be that some star-formation occurs in regions where no $H\alpha$ photons are able to escape, and therefore such star-formation would be missing in an optically-based SFR census.

3.5. Star-forming knots and diffuse emission

This section presents the results concerning the analysis of the spatial distribution and intensity of the star formation in the UCM galaxies. This study has two main goals: (1) to segregate the star-forming knots from the regions with a more diffuse ionized gaseous component (DIG), and (2) to characterize the regions with active star formation.

3.5.1. Detection method

In order to separate the distinct star-forming knots from the diffuse emission, we have followed a similar method to the one used by Rozas et al. (1996) and Zurita (2001) to detect HII regions and study their luminosity functions in nearby galaxies. The main difference is that, due to their higher distances, the angular sizes of the UCM galaxies are much smaller than those of the galaxies studied by these authors. Thus, the average spatial resolution element of our H α imaging study (i.e., the diameter of the typical seeing disk, $\sim 1''$) corresponds to ~ 0.5 kpc. This value is similar to the diameters of the largest HII regions found in nearby galaxies (~ 400 pc, Youngblood & Hunter 1999; Zurita 2001). Therefore, the star-forming regions detected in our sample correspond to large star-forming complexes rather than normal HII regions. Moreover, the UCM objects present enhanced star formation in comparison with normal quiescent galaxies. This behavior also has an effect on the size and intensity of the starbursts.

The detection method of the star-forming knots deals with four different issues:

- 1.– The global limit for the detection of any feature was set to 2 times the noise level of the sky background.
- 2.– The criterion for distinguishing an individual star-forming knot from its neighbors was that every local maximum with no other maxima closer than 2 pixels was considered as an individual knot. This separation was chosen so that the diameter of any knot would be at least as large as the average diameter of the seeing disk in our frames ($\sim 1'' = 5$ pixels).
- 3.– The technique used to decide which pixels belong to each region when there are other regions nearby is described in Zurita (2001). The technique is based on the same principles used by the SExtractor software (Bertin & Arnouts 1996) to de-blend objects.
- 4.– The detection limit for the boundaries (faintest parts) of the star-forming regions was chosen to coincide with the upper intensity limit for the diffuse emission (see ahead).

The value we used was $1.32 \times 10^{-16} \text{ erg s}^{-1} \text{ cm}^{-2} \text{ arcsec}^{-2}$. The limit corresponds to an emission measure⁶ $EM = 65 \text{ pc cm}^{-6}$. The choice of this value is based on several studies of the diffuse ionized medium in spiral galaxies (for example, Ferguson et al. 1996a,b use a cutoff value of 80 pc cm^{-6} , and Hoopes et al. 1996 use 50 pc cm^{-6}).

3.5.2. Star-forming knots

In the 79 galaxies included in the present study, we have detected 816 distinct star-forming knots. The number of regions found in each galaxy ranges widely, from one single region per galaxy to up to 87 regions for one galaxy (UCM2325+2318, a luminous infrared galaxy, Calzetti et al. 2000). The median value is ~ 8 regions per galaxy. We detect more regions in late-type spirals and interacting systems (on average, 12 regions in Sc+ galaxies, 18 in Irr and 45 in interacting systems) than in early-type spirals (5–8 for S0/Sb) and BCDs (1 region).

Interestingly, no strong correlation is observed between the number of regions detected within an object and the distance to the galaxy. The Spearman’s rank correlation coefficient for these parameters is 0.2, with a two-sided significance level of its deviation from 0 of 4×10^{-2} . This indicates that, with our definition of star-forming knots, spatial resolution is not a major factor in the number of star-forming knots detected for the range of distances covered by the UCM galaxies. In contrast, the number of regions and the apparent size of the entire galaxy (taken as the radius of the 24.5 mag arcsec⁻² isophote) do show some correlation: larger galaxies tend to have more star-forming regions. The Spearman’s rank correlation coefficient of these quantities is 0.48 and the two-sided significance level of its deviation from 0 is 7×10^{-6} . In addition, those galaxies with large numbers of regions are also more luminous than objects with fewer knots of star formation.

The median radius of the star-forming knots in the UCM galaxies is 0.5 kpc, which is approximately twice the average resolution (cf. Section 3.5.1). The smallest detected knot has a radius of $\sim 100 \text{ pc}$. The starburst complexes can be as large as 4 kpc. The most extreme cases are found in UCM1513+2012 and UCM2250+2427, two very disturbed galaxies.

⁶The emission measure EM , whose units are pc cm^{-6} , is defined as $EM = \int_0^d N_e^2 ds$, where N_e is the electron density and the integral extends to the line of sight. For an electron temperature of $T = 10^4 \text{ K}$, $EM = 4.908 \times 10^{17} \text{ I(H}\alpha\text{)}$, where $\text{I(H}\alpha\text{)}$ is the intensity in $\text{erg s}^{-1} \text{ cm}^{-2} \text{ arcsec}^{-2}$.

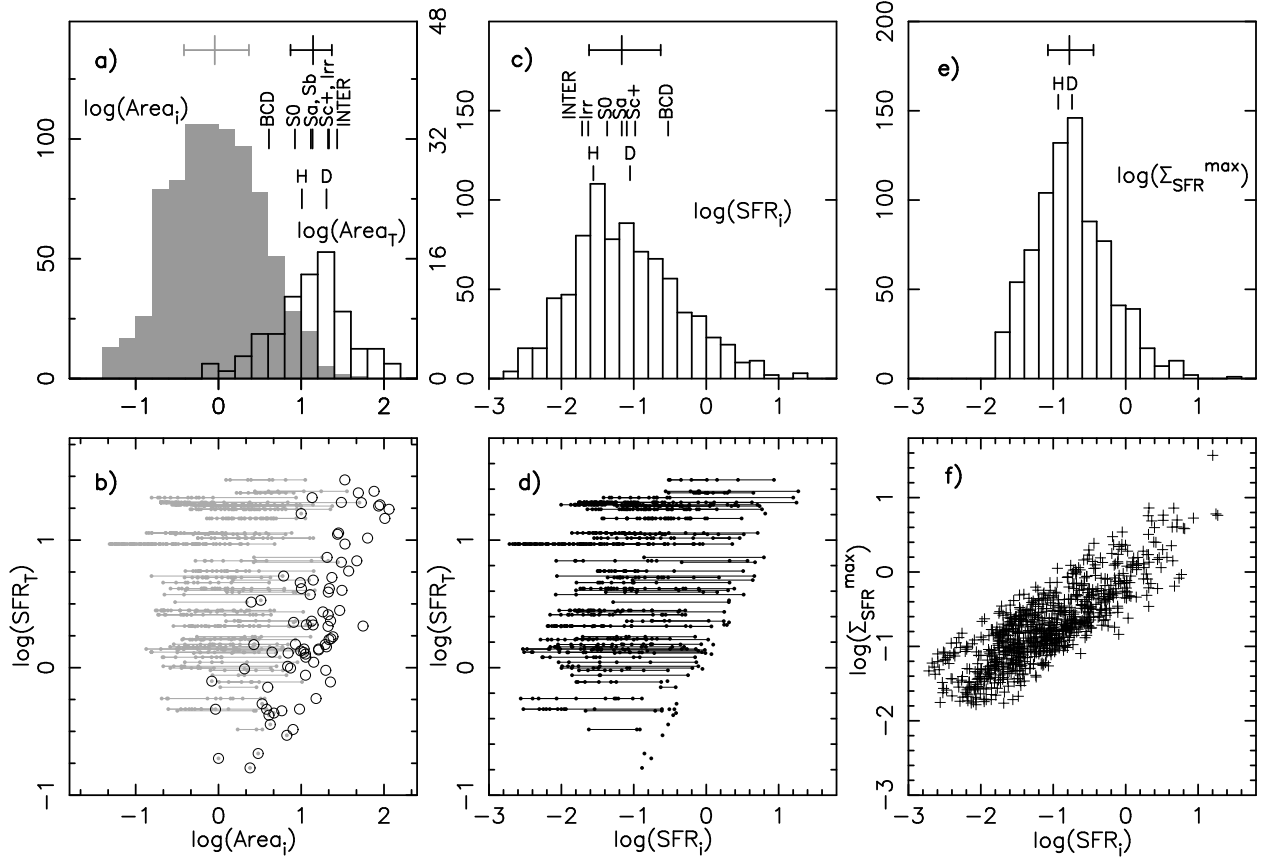


Fig. 9.— Frequency distributions and correlations of the properties of the star-forming knots detected in the UCM sample. Areas are in kpc^2 , SFRs in $\mathcal{M}_\odot \text{ yr}^{-1}$, and $\Sigma_{\text{SFR}}^{\text{max}}$ in $\mathcal{M}_\odot \text{ yr}^{-1} \text{ kpc}^{-2}$. Panels show: a) Histograms of the area of the individual star-forming knots (Area_i , in gray) and the total extension of the $\text{H}\alpha$ emission (Area_T). Median values and quartiles of the entire distributions are marked by the error bars. The median values for the different morphological and spectroscopic classes are also marked. b) Relationship between the global SFR and the extension of the $\text{H}\alpha$ emission. Data for the individual knots are plotted with gray points. A horizontal gray line joins the knots belonging to the same galaxy (when more than one knot have been detected). Data referring to the integrated area of the $\text{H}\alpha$ emission are depicted with open circles. c) Distribution of the SFRs of individual star-forming knots within the UCM galaxies. Median values and quartiles of the entire distribution and for each morphological and spectroscopic types are marked. d) Relationship between the global SFR and the SFR of the individual knots. A horizontal line joins the knots belonging to the same galaxy (when more than one knot have been detected). e) Distribution of the maximum surface density of SFR ($\Sigma_{\text{SFR}}^{\text{max}}$; see text). Median values and quartiles of the entire distribution and different spectroscopic types are marked. And f) $\Sigma_{\text{SFR}}^{\text{max}}$ vs. SFR_i for the detected star-forming knots in the UCM sample.

Using the conversion factor given in Equation 3 we have also calculated global SFRs (SFR_T), average SFR surface densities (Σ_{SFR}), and maximum SFR surface densities ($\Sigma_{\text{SFR}}^{\text{max}}$, the SFR surface density of the pixel with the highest intensity) for each of the regions.

The gray histogram in Figure 9(a) shows the frequency distribution of the surface areas of the individual star-forming knots. The projected areas range from 0.05 to 50 kpc^2 . The distribution peaks at $\sim 1 \text{ kpc}^2$, with a median value of 0.9 kpc^2 . The frequency distribution of the total area of the $\text{H}\alpha$ -emitting regions in each galaxy is also shown (empty histogram). This distribution presents a peak at $\sim 14 \text{ kpc}^2$. Median values for the different morphological and spectroscopic types are marked. A trend is observed in the sense that later Hubble types have larger active star-forming areas. As expected for their dwarf nature, BCDs are characterized by the small extension of the burst zone. On the contrary, the objects that were classified as highly-disturbed interacting systems present the most extended bursts (the median is 27 kpc^2). From a spectroscopic point of view, *disk-like* galaxies show emitting total areas which are twice the size of those of *HII-like* objects.

Figure 9(b) shows the correlation between the total area covered by the $\text{H}\alpha$ emission and the SFR of the galaxy (open circles). Data for the individual regions in each galaxy is also shown as dots joined by a line. The total area covered by star-formation in each galaxy is reasonably well correlated to the total SFR, and the logarithmic slope of the relation is close to 1. This indicates that the range in global SFR surface densities is relatively narrow for all the galaxies in the UCM sample. Indeed, the median value of the total SFR per unit star-forming area in the UCM sample is $0.15 \mathcal{M}_{\odot} \text{ yr}^{-1} \text{ kpc}^{-2}$, with an rms of only 0.4dex. Note that since these numbers have not been corrected for inclination, the intrinsic scatter is probably smaller. Interestingly, we also find the most extended individual knots in the most actively star-forming galaxies (see discussion of Figure 9(d) below).

Figure 9(c) shows the frequency distribution of the SFRs estimated for the individual regions. Median values for the global distribution and for each morphological and spectroscopic types are shown. There is, again, a clear trend with morphology for the spiral galaxies: later types have more intense star-forming knots than earlier spirals. BCDs are segregated from the rest of the galaxies since they tend to have the brightest star-forming regions. Somewhat surprisingly, irregular and interacting galaxies seem to have star-forming regions with lower individual SFRs, but since, as we found before, they tend to have large numbers of them, their global SFRs can still be high. The star-forming knots in *disk-like* galaxies are also more intense (by a factor of a few) than those found in *HII-like* objects. This seems to suggest two different star-formation regimes operate in ‘quiescent’ objects (e.g., normal spirals) and disturbed/interacting objects.

Figure 9(d) shows that high integrated $\text{H}\alpha$ emission in a galaxy is accompanied by the

existence of more intense individual star-forming regions. This trend may be explained in part by an statistical effect. If the frequency distribution shown in figure 9(c) is sampled randomly in each galaxy, the most intense star-forming knots would tend to appear in galaxies with large SFRs. In some cases, galaxies with low SFR will be completely dominated by one single burst. However, if two different star-formation regimes operate in disturbed and ‘quiescent’ galaxies, this simple statistical explanation would be complicated by the possible existence of different frequency distributions for the different star-formation modes. Moreover, simple statistics do not provide the whole story. In a significant fraction of the galaxies where multiple star-forming knots are found, the global star formation is completely dominated by one of them (often the central/nuclear one; cf. section 3.2). Obviously, this also contributes to the observed correlation.

Finally, figure 9(f) presents the tight correlation existing between the SFR of individual star-forming knots and their maximum Σ_{SFR} . A similar behaviour is observed between the average Σ_{SFR} of each knot and the total SFR, though a larger scatter is found. The values of the maximum Σ_{SFR} that we find are lower than the maximum limit found for starbursts by Meurer et al. (1997), which is consistent with the fact that most of our galaxies are not extreme starbursts. We observe no correlation between $\Sigma_{\text{SFR}}^{\text{max}}$ (or Σ_{SFR}) and morphological type.

Summarizing the results shown in figure 9, the most intense star-forming knots present the highest SFR surface densities and largest sizes. These properties eventually translate into a larger global H α emission for the entire galaxy. High-resolution studies have also found this correlation between the global SFR and the number and mass of the individual star-forming knots (see Kennicutt 1998a, and references therein). Even though these trends apply to the vast majority of the UCM galaxies, we also find suggestive evidence that a different star-formation mode could be operating in the irregular/interacting galaxies in our sample.

3.5.3. Diffuse H α emission

We have followed two different approaches when separating the diffuse ionized gas (DIG) emission from the star-forming knots. First, we used an absolute surface brightness cutoff value that corresponds to the faintest emission that we considered to be part of a star-formation knot in the previous section ($1.32 \times 10^{-16} \text{ erg s}^{-1} \text{ cm}^{-2} \text{ arcsec}^{-2}$). Such an approach does not deal with spatial variations of the DIG intensity within a galaxy or from one object to another. For that reason, we have also used a more elaborated detection technique that takes into consideration distinctive properties of the DIG such as its diffuseness or

its morphology. Following Zurita (2001), we have built gradient maps of the $H\alpha$ flux to select the zones presenting the lowest spatial variations of the emission. These zones were identified with the diffuse ionized gas. The selected upper limits of the intensity gradient that we used are very similar to the values used by Zurita (2001): the median for our sample is $45 \text{ pc cm}^{-6} \text{ arcsec}^{-1}$ and Zurita used $44 \text{ pc cm}^{-6} \text{ arcsec}^{-1}$. We will discuss the results obtained with both methods in this section.

Using both detection methods, diffuse emission has been detected in all but 5 galaxies for an upper intensity cutoff of 65 pc cm^{-6} . The median intensity of the DIG is 46 pc cm^{-6} . This value is typical of the brightest component of the DIG observed in nearby galaxies (3-5 times larger than the averages given in Hoopes et al. 1996 and Zurita 2001).

The comparison of the flux arising from the diffuse ionized gas and the total $H\alpha$ emission of the galaxy provides a useful diagnostic of the escape of Lyman photons from HII regions. These photons may ionize the gas in the disks of the galaxies or even escape to the intergalactic medium. In both cases, it would be necessary to revise the assumptions made when linking the measured emission from HII regions to SFR, and when dealing with interaction between active star formation and the interstellar and intergalactic medium.

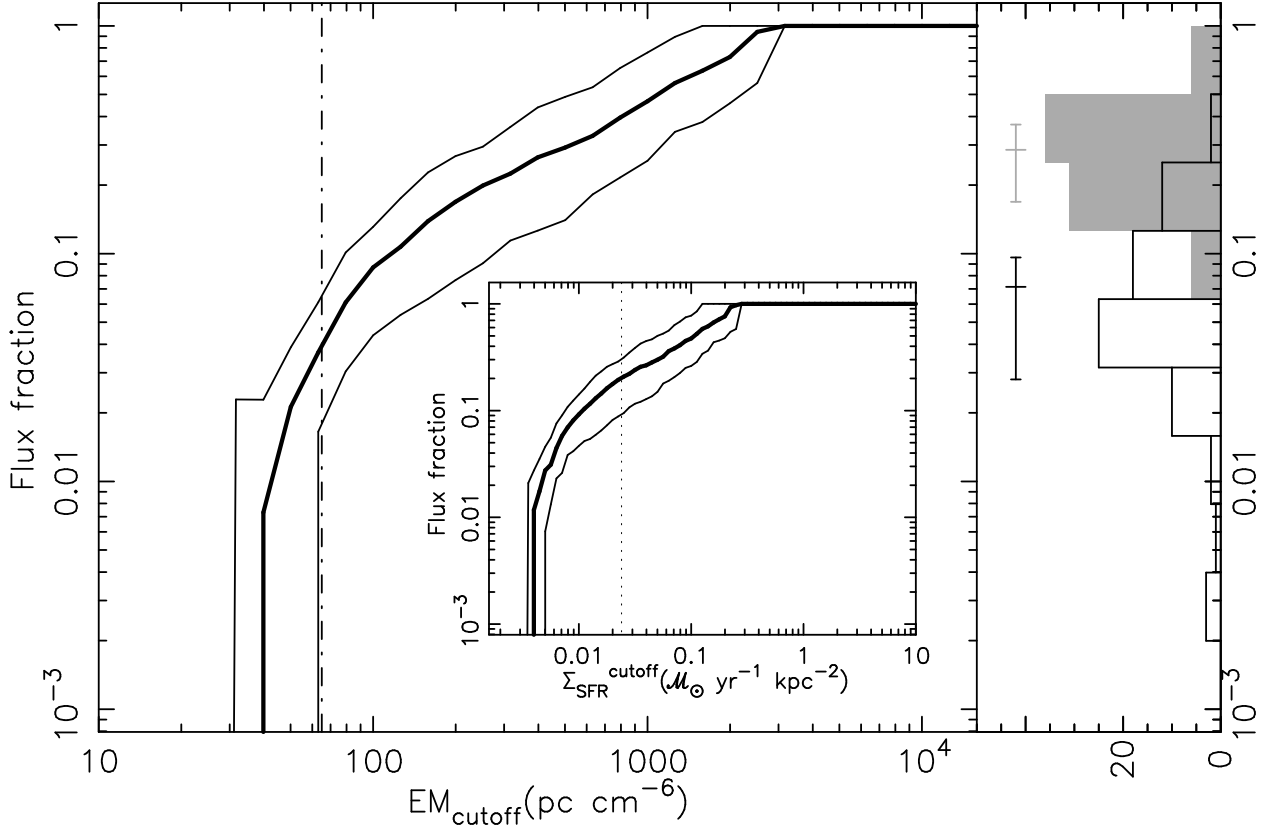


Fig. 10.— Median contribution of the different intensity levels of the H α emission to the total flux for the galaxies in the UCM sample (left panel). The flux fraction (vertical axis) refers to the contribution to the total flux of the emission regions with an intensity below a given surface brightness cutoff (horizontal axis). The median value for the entire sample at each cutoff intensity is shown (thick line) together with the upper and lower quartiles (thin line). The inset plot depicts the same flux ratio against the SFR surface density levels. For comparison, the Σ_{SFR} limit for the survey of $z \sim 0.24$ galaxies published by Pascual et al. (2001) is marked with a dotted line (see text). The right panel presents the histogram of the DIG fraction of the total flux (calculated using the pixels whose intensity is over the global detection limit) for an EM cutoff of 65 pc cm^{-6} (empty histogram). The gray histogram shows the same fraction but corrected for the DIG over-imposed in the star-forming knots.

In order to characterize the DIG in the UCM galaxies, the contribution to the total flux of the emission zones with an intensity below a certain surface brightness cutoff has been measured. Figure 10 plots this quantity against the cutoff intensity. The median values for the 79 galaxies in our sample are shown, together with the first and third quartiles. The upper cutoff value for the DIG (65 pc cm^{-6}) is shown.

The right panel of Figure 10 shows a histogram of the fractional contribution of the DIG to the $\text{H}\alpha$ fluxes. Individual values range from 0% to 34% (UCM1308+2950). On average, 8% of the total $\text{H}\alpha$ flux of a UCM galaxy comes from pixels that were identified as DIG. Only pixels with fluxes over the global detection limit were used in this calculation.

When using the gradient method explained above to detect the DIG emission, we get very similar results. These figures are consistent with previous studies on the DIG properties (e.g, Hoopes et al. 1996; Wang et al. 1999; Zurita 2001) and on the escape of Lyman photons from HII regions (Oey & Kennicutt 1997).

These results do not take into account the effects of the light scattered by the dust in the galaxies or by the optics of the telescope. The correction for these effects has been estimated to be 5–15% of the diffuse flux by Hoopes et al. (1996). In addition, the fluxes in Figure 10 (left panel) do not contain the contribution of the DIG located in the line of sight of the star-forming regions, i.e., superimposed on them. We have estimated the correction factor for this effect by substituting the intensity of the pixels belonging to a star-forming knot by the average value of the detected DIG pixels. This correction rises the DIG contribution to the total flux by a factor of ~ 2 . These factors are consistent with the ones found by Hoopes et al. (1996). The histogram for the flux fraction of the DIG corrected for these effects has also been plotted in the right panel of Figure 10 (gray histogram).

We do not find large differences between the flux fraction of the DIG for different morphologies. If anything, Sa galaxies show a somewhat lower fraction ($\sim 10\%$, including the corrections mentioned above) when compared with later Hubble types (20%). Interacting systems and BCDs present somewhat lower fractions. For the different spectroscopic classes, we find that *disk-like* galaxies show larger fractions ($\sim 20\%$) than *HII-like* objects (less than 10%).

Imaging surveys of galaxies at intermediate and high redshifts are able to detect emission-line objects to a certain flux limit which can be expressed in units of SFR surface density ($\mathcal{M}_{\odot} \text{ yr}^{-1} \text{ kpc}^{-2}$). This obviously means that objects that are fainter than that limit are not detected. But even for objects that are detected, a significant fraction of the total flux may be under the detection limit and thus missed. To estimate how important this effect may be, we have calculated the ratio of the luminosity arising from regions with a SFR surface density

below a given cutoff value to the integrated luminosity, i.e., the cumulative contribution of the different SFR surface density levels to the total SFR. Here we have calculated the total emission for these objects adding the flux in all pixels above the detection limit. The inset in Figure 10 shows the results of this calculation. Under the assumption that the distant galaxies under consideration are comparable to the UCM galaxies in their star formation properties and spatial distribution, this plot gives a correction to the detected luminosity for each detection limit. As an example we refer to the survey of $z \sim 0.24$ H α emitting galaxies published by Pascual et al. (2001). The faintest galaxy in this survey has an H α luminosity of 3.4×10^{41} erg s $^{-1}$ measured in a circular aperture of $1.6''$ or ~ 100 kpc 2 . This turns into an average SFR surface density of $\sim 0.02 \mathcal{M}_{\odot} \text{ yr}^{-1} \text{ kpc}^{-2}$, which is shown in Figure 10. If we assume this value as the detection limit, this figure reveals that the survey was missing about 20% of the total H α flux in pixels with an intensity below the detection limit. Similar corrections may be calculated for other surveys.

3.6. H α luminosity function and the SFR density of the Universe

The integrated luminosities measured in the H α images can be used to recalculate the luminosity function and the star formation rate density of the local Universe first published by Gallego et al. (1995). In that paper, the H α fluxes measured in the spectra were converted to luminosities after an aperture correction. This correction assumed that the $EW(\text{H}\alpha)$ was constant over the whole galaxy, and used integrated Gunn- r magnitudes and the spectroscopic $EW(\text{H}\alpha)$ values to estimate H α luminosities. We compare these luminosities with the ones measured in the H α images in Figure 11. In the inset of that figure we also present the histograms of the frequency distributions of the imaging and spectroscopic luminosities (empty and gray histograms respectively). Median values and upper/lower quartiles are indicated.

We find that, statistically, the luminosities estimated from the spectroscopic data worked quite well. On average, the aperture-corrected spectroscopic data underestimated the total emission of the UCM Survey galaxies by $\simeq 10\%$ only (the corresponding median value is 30%). However, Figure 11 shows that on an individual galaxy basis, the spectroscopic estimates can be off by factors of up to a few. Note that galaxy sizes are not the determinant factor on the accuracy of the aperture correction. The key factor is how valid the spectroscopically-determined $EW(\text{H}\alpha)$ value is for the whole galaxy.

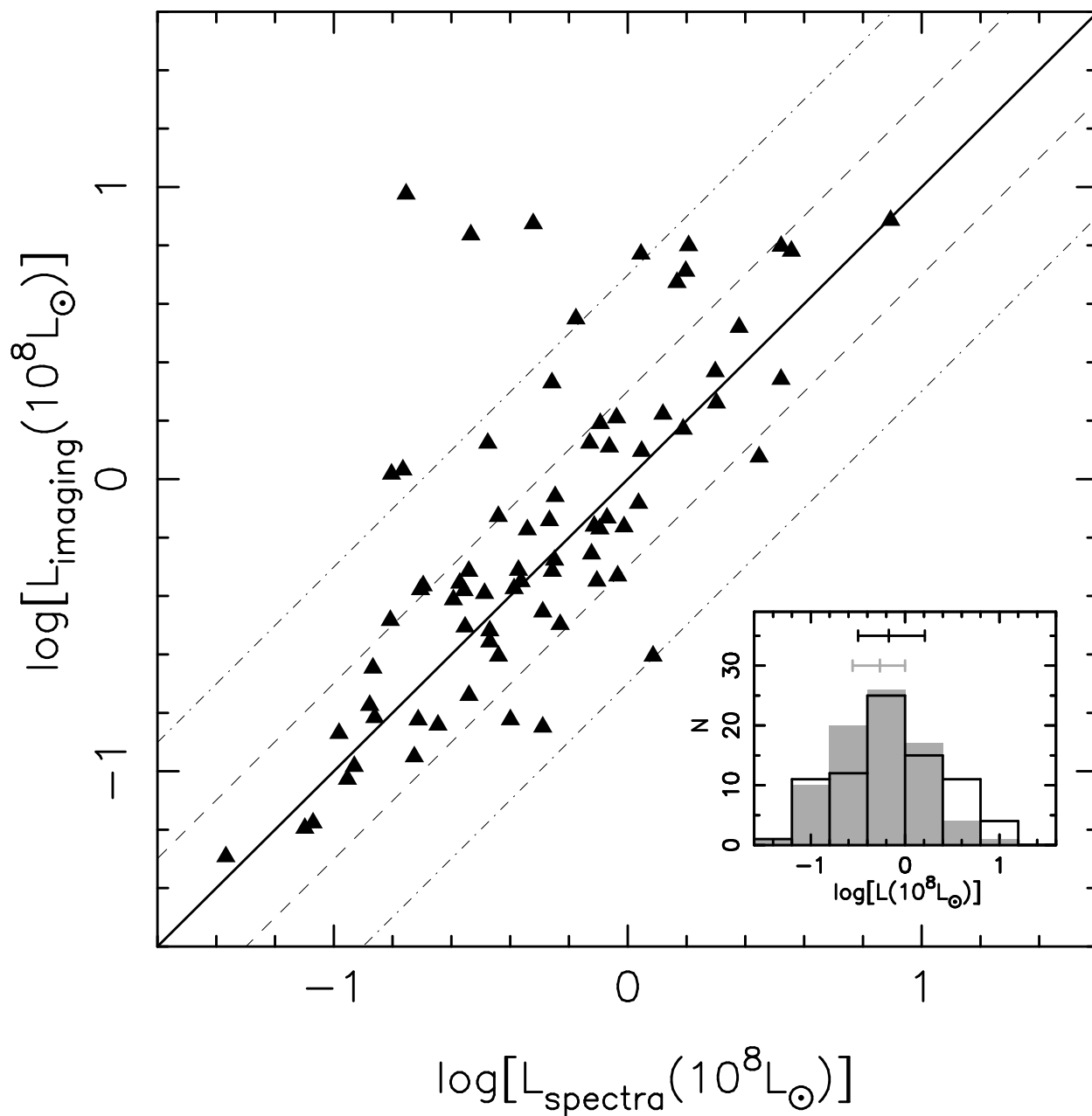


Fig. 11.— Comparison of the $H\alpha$ luminosities obtained from spectroscopy (aperture corrected) and imaging. The dashed lines correspond to factors of 5, 2, 1/2 and 1/5. The inset plot shows the frequency histograms for the imaging (empty) and spectroscopic (gray) luminosities.

We have now recalculated the H α luminosity function and the SFR density of the local Universe using the imaging-based luminosities corrected for internal extinction. We have assumed that the galaxies in our H α imaging sample are a fair subsample of the entire UCM survey with regard to their H α luminosities (cf. section Section 2), and we have followed the same techniques of the original work of Gallego et al. (1995). For direct comparison with the spectroscopic study, this analysis is carried out for a cosmology with $H_0 = 50 \text{ km s}^{-1} \text{ Mpc}^{-1}$, $\Omega_M = 1$ and $\Lambda = 0$ as well as for the cosmology used elsewhere in this paper ($H_0 = 70$; $\Omega_M = 0.3$; $\Lambda = 0.7$). Using the V/V_{max} method (Schmidt 1968; Huchra & Sargent 1973), the Schechter parameters of the best fit are:

$$\begin{array}{ll}
 (H_0 = 50, \Omega_M = 1.0, \Lambda = 0.0) & (H_0 = 70, \Omega_M = 0.3, \Lambda = 0.7) \\
 \\
 \alpha = -1.1 \pm 0.2 & \alpha = -1.2 \pm 0.2 \\
 \phi^* = 10^{-3.3 \pm 0.2} \text{ Mpc}^{-3} & \phi^* = 10^{-3.0 \pm 0.2} \text{ Mpc}^{-3} \\
 L^* = 10^{42.60 \pm 0.20} \text{ erg s}^{-1} & L^* = 10^{42.43 \pm 0.17} \text{ erg s}^{-1}
 \end{array}$$

Similar results (within the uncertainties) have been obtained using the two more sophisticated luminosity function estimators developed by Sandage et al. (1979) and Efstathiou et al. (1988). The main difference found with the spectroscopic results is that the characteristic H α luminosity L^* of a local star-forming galaxy is a factor of ~ 3 brighter in the imaging-based study than in the spectroscopic one. The reason for this appears to be that the H α images have revealed that several large and H α -bright objects had their luminosities underestimated by the spectroscopic data because their star formation was mainly located away from the nuclear regions sampled by the slits (cf. figure 11). Similar results have been found recently by Serjeant et al. (2002), based on radio observations.

The total H α luminosity density of the local Universe can be calculated by integrating the luminosity function for all luminosities. This yields values of $10^{39.3 \pm 0.2} \text{ erg s}^{-1} \text{ Mpc}^{-3}$ ($H_0 = 50$; $\Omega_M = 1$; $\Lambda = 0$) and $10^{39.5 \pm 0.2} \text{ erg s}^{-1} \text{ Mpc}^{-3}$ for the ‘concordance cosmology’. For a fixed cosmology, the imaging-based density is $\sim 60\%$ (0.2dex) larger than the spectroscopic one of Gallego et al. (1995), but note that the formal uncertainty in the measured value is also 0.2dex.

Using the transformation from L(H α) to SFR given in Equation 3, we obtain the SFR density of the local Universe: $\rho_{SFR} = 0.016_{-0.004}^{+0.007} \mathcal{M}_\odot \text{ yr}^{-1} \text{ Mpc}^{-3}$ ($H_0 = 50$; $\Omega_M = 1$; $\Lambda = 0$) and $\rho_{SFR} = 0.029_{-0.005}^{+0.008} \mathcal{M}_\odot \text{ yr}^{-1} \text{ Mpc}^{-3}$ ($H_0 = 70$; $\Omega_M = 0.3$; $\Lambda = 0.7$)⁷.

⁷Note that the value of the SFR density given in Gallego et al. (1995) ($0.013 \mathcal{M}_\odot \text{ yr}^{-1} \text{ Mpc}^{-3}$ for $H_0 = 50$; $\Omega_M = 1$; $\Lambda = 0$) was obtained with a different transformation factor from H α luminosity to SFR, so the

4. Summary and conclusions

In this paper we have presented H α images for a statistically-representative subsample of 79 local star-forming galaxies. This sample has been selected from the UCM Survey galaxies ensuring that the distributions of H α luminosities, equivalent widths and spectroscopic types are representative of the entire survey. The observations, data reduction and analysis have been described, and we have presented results concerning galaxy properties such as their concentration, bulge and disk emission, relationship between newly-formed stars and underlying older population, distribution of star-forming knots and properties of the diffuse emission. We have also discussed the implications of our imaging survey on the determination of the local H α luminosity function and star formation rate density. The main results of this work are:

- 1.– Typical long-slit or fiber spectroscopic observations of nearby galaxies such as those in the UCM sample ($\langle z \rangle = 0.026$) can miss substantial fractions of the emission-line flux (typically 50%–70%). Thus, to avoid applying uncertain aperture corrections, direct emission-line imaging (e.g., narrow-band H α imaging) can provide useful and complementary information to spectroscopy.
- 2.– The average concentration parameter c_{31} (Gavazzi et al. 1990) of the UCM Survey galaxies is typical of disk dominated galaxies. Its distribution peaks at $c_{31} \sim 3$. The average size of the emission regions is ~ 1.5 kpc, but this size correlates with morphology in the sense that late-type spirals have significantly larger H α -emitting regions than early types. On average, the star formation event covers half of the total size of these galaxies.
- 3.– Using a technique akin to bulge/disk decomposition for the H α radial distribution we have robustly separated the contribution to the total emission into nuclear and disk components. On average, a UCM galaxy harbors a star formation event with a nuclear component contributing 30% of its line emission. A significant disk emission component is detected in the vast majority of the galaxies, including objects that were spectroscopically classified as *starburst nuclei*.
- 4.– In contrast with previous studies, we do not find a correlation between the H α equivalent width and Hubble type for spirals. This may be a consequence of the enhanced star-forming activity of the UCM galaxies (H α -selected) with respect to broad-band

values are not directly comparable. The correct comparison needs to be carried out for the H α luminosity densities, as we have done above.

selected ones: our sample is dominated by high- $EW(H\alpha)$ galaxies. Disk-*like* galaxies present considerable lower values of the $EW(H\alpha)$ (24 Å) than HII-*like* objects (75 Å). This suggests that the underlying older stellar population in disk-*like* galaxies has a larger relative contribution to the galaxy luminosity than in HII-*like* objects.

- 5.– A positive correlation between the SFR and the extinction has been found, although the correlation seems to saturate for heavily-obscured objects ($H\alpha/H\beta \gtrsim 7$ corresponding to $E(B - V) \gtrsim 0.9$). This suggests that in objects with very high extinction a large fraction of the SFR could be completely hidden by dust with the Balmer line ratio only tracing those regions with the lowest (but still high) extinction.
- 6.– The most intense star-forming knots in the UCM galaxies present the highest SFR surface densities and largest sizes. Moreover, the brightest and largest star-forming knots are found in galaxies with the highest $H\alpha$ luminosities. We have also found some evidence for the existence of two different star-formation regimes operating in ‘quiescent’ objects (e.g., normal spirals) and disturbed/interacting/irregular objects: the latter seem to have, on average, star-forming regions with lower individual SFRs, but larger numbers of them so that their global SFRs can still be relatively high.
- 7.– About 15–30% of the total $H\alpha$ flux of a typical UCM galaxy comes from a diffuse ionized gas component. This percentage seems to be independent of the Hubble type.
- 8.– The present $H\alpha$ imaging study has led to the recalculation of the $H\alpha$ luminosity function and star formation rate density of the local Universe. Our results yield an $H\alpha$ luminosity density in the local Universe of $10^{39.3\pm 0.2} \text{ erg s}^{-1} \text{ Mpc}^{-3}$ ($H_0 = 50$; $\Omega_M = 1$; $\Lambda = 0$) and $10^{39.5\pm 0.2} \text{ erg s}^{-1} \text{ Mpc}^{-3}$ ($H_0 = 70$; $\Omega_M = 0.3$; $\Lambda = 0.7$). For a fixed cosmology, these values are 60% larger than the densities calculated in Gallego et al. (1995). These luminosity densities translate into SFR densities of $\rho_{SFR} = 0.016_{-0.004}^{+0.007} \mathcal{M}_\odot \text{ yr}^{-1} \text{ Mpc}^{-3}$ ($H_0 = 50$; $\Omega_M = 1$; $\Lambda = 0$) and $\rho_{SFR} = 0.029_{-0.005}^{+0.008} \mathcal{M}_\odot \text{ yr}^{-1} \text{ Mpc}^{-3}$ ($H_0 = 70$; $\Omega_M = 0.3$; $\Lambda = 0.7$).

PGPG wishes to acknowledge the Spanish Ministry of Education and Culture for the reception of a *Formación de Profesorado Universitario* fellowship. AAS acknowledges generous financial support from the Royal Society. AGdP acknowledges financial support from NASA through a Long Term Space Astrophysics grant to B.F. Madore. Valuable discussion with Almudena Zurita is acknowledged. We are grateful to the anonymous referee for her/his helpful comments and suggestions. The present work was supported by the Spanish Programa Nacional de Astronomía y Astrofísica under grant AYA2000-1790.

REFERENCES

- Alonso, O., García-Dabó, C. E., Zamorano, J., Gallego, J., & Rego, M. 1999, *ApJS*, 122, 415
- Balzano, V. A. 1983, *ApJ*, 268, 602
- Bell, E. F. 2002, *ApJ*, 577, 150
- Bertin, E. & Arnouts, S. 1996, *A&AS*, 117, 393
- Calzetti, D., Armus, L., Bohlin, R. C., Kinney, A. L., Koornneef, J., & Storchi-Bergmann, T. 2000, *ApJ*, 533, 682
- Cardelli, J. A., Clayton, G. C., & Mathis, J. S. 1989, *ApJ*, 345, 245
- Chitre, A. & Joshi, U. C. 2001, *Journal of Astrophysics and Astronomy*, 22, 155
- Combes, F. . 2001, in *ASP Conf. Ser. 249: The Central Kiloparsec of Starbursts and AGN: The La Palma Connection*, 475
- Conselice, C. J., Bershad, M. A., & Gallagher, J. S. 2000a, *A&A*, 354, L21
- Conselice, C. J., Gallagher, J. S., Calzetti, D., Homeier, N., & Kinney, A. 2000b, *AJ*, 119, 79
- Davidge, T. J. 1992, *AJ*, 103, 1512
- de Vaucouleurs, G. 1948, *Annales d’Astrophysique*, 11, 247
- Efstathiou, G., Ellis, R. S., & Peterson, B. A. 1988, *MNRAS*, 232, 431
- Ellis, R. S., Colless, M., Broadhurst, T., Heyl, J., & Glazebrook, K. 1996, *MNRAS*, 280, 235
- Ferguson, A. M. N., Wyse, R. F. G., & Gallagher, J. S. 1996a, *AJ*, 112, 2567
- Ferguson, A. M. N., Wyse, R. F. G., Gallagher, J. S., & Hunter, D. A. 1996b, *AJ*, 111, 2265
- Freeman, K. C. 1970, *ApJ*, 160, 811
- Fukugita, M., Shimasaku, K., & Ichikawa, T. 1995, *PASP*, 107, 945
- Gallego, J. 1995, PhD thesis, Universidad Complutense de Madrid
- . 1998, *Ap&SS*, 263, 1

- Gallego, J., García-Dabó, C. E., Zamorano, J., Aragón-Salamanca, A., & Rego, M. 2002, ApJ, 570, L1
- Gallego, J., Zamorano, J., Aragón-Salamanca, A., & Rego, M. 1995, ApJ, 455, L1
- Gallego, J., Zamorano, J., Rego, M., Alonso, O., & Vitores, A. G. 1996, A&AS, 120, 323
- Gallego, J., Zamorano, J., Rego, M., & Vitores, A. G. 1997, ApJ, 475, 502
- Gavazzi, G., Catinella, B., Carrasco, L., Boselli, A., & Contursi, A. 1998, AJ, 115, 1745
- Gavazzi, G., Garilli, B., & Boselli, A. 1990, A&AS, 83, 399
- Gil de Paz, A., Aragón-Salamanca, A., Gallego, J., Alonso-Herrero, A., Zamorano, J., & Kauffmann, G. 2000, MNRAS, 316, 357
- Goldader, J. D., Meurer, G., Heckman, T. M., Seibert, M., Sanders, D. B., Calzetti, D., & Steidel, C. C. 2002, ApJ, 568, 651
- González Delgado, R. M., Leitherer, C., & Heckman, T. M. 1999, ApJS, 125, 489
- Guzmán, R., Gallego, J., Koo, D. C., Phillips, A. C., Lowenthal, J. D., Faber, S. M., Illingworth, G. D., & Vogt, N. P. 1997, ApJ, 489, 559
- Haarsma, D. B., Partridge, R. B., Windhorst, R. A., & Richards, E. A. 2000, ApJ, 544, 641
- Hameed, S. & Devereux, N. 1999, AJ, 118, 730
- Hamuy, M., Walker, A. R., Suntzeff, N. B., Gigoux, P., Heathcote, S. R., & Phillips, M. M. 1992, PASP, 104, 533
- Hogg, D. W., Cohen, J. G., Blandford, R., & Pahre, M. A. 1998, ApJ, 504, 622
- Hoopes, C. G., Walterbos, R. . M., & Bothun, G. D. 2001, ApJ, 559, 878
- Hoopes, C. G., Walterbos, R. A. M., & Greenwalt, B. E. 1996, AJ, 112, 1429
- Hopkins, A. M., Connolly, A. J., Haarsma, D. B., & Cram, L. E. 2001, AJ, 122, 288
- Huchra, J. & Sargent, W. L. W. 1973, ApJ, 186, 433
- Iglesias-Páramo, J. & Vílchez, J. M. 1999, ApJ, 518, 94
- Jarrett, T. H., Chester, T., Cutri, R., Schneider, S., Skrutskie, M., & Huchra, J. P. 2000, AJ, 119, 2498

- Jones, D. H. & Bland-Hawthorn, J. 2001, *ApJ*, 550, 593
- Kauffmann et al. 2002, *MNRAS* (in press), astro-ph/0204055
- Kennicutt, R. C. 1983, *ApJ*, 272, 54
- . 1989, *ApJ*, 344, 685
- . 1998a, *ARA&A*, 36, 189
- . 1998b, *ApJ*, 498, 541
- Kennicutt, R. C., Bothun, G. D., & Schommer, R. A. 1984, *AJ*, 89, 1279
- Kennicutt, R. C. & Kent, S. M. 1983, *AJ*, 88, 1094
- Kennicutt, R. C., Tamblyn, P., & Congdon, C. E. 1994, *ApJ*, 435, 22
- Landolt, A. U. 1992, *AJ*, 104, 340
- Lanzetta, K. M., Yahata, N., Pascarelle, S., Chen, H., & Fernández-Soto, A. 2002, *ApJ*, 570, 492
- Lehnert, M. D. & Heckman, T. M. 1994, *ApJ*, 426, L27
- . 1996, *ApJ*, 472, 546
- Lilly, S. J., Le Fevre, O., Hammer, F., & Crampton, D. 1996, *ApJ*, 460, L1
- Madau, P., Pozzetti, L., & Dickinson, M. 1998, *ApJ*, 498, 106
- Meurer, G. R., Heckman, T. M., Lehnert, M. D., Leitherer, C., & Lowenthal, J. 1997, *AJ*, 114, 54
- Oey, M. S. & Kennicutt, R. C. 1997, *MNRAS*, 291, 827
- Oke, J. B. 1990, *AJ*, 99, 1621
- Pérez-González, P. G., Gil de Paz, A., Zamorano, J., Gallego, J., Alonso-Herrero, A., & Aragón-Salamanca, A. 2003a, *MNRAS*, 338, 508
- . 2003b, *MNRAS*, 338, 525
- Pérez-González, P. G., Zamorano, J., & Gallego, J. 2001, in *Highlights of Spanish astrophysics II*, 97

- Pascual, S., Gallego, J., Aragón-Salamanca, A., & Zamorano, J. 2001, *A&A*, 379, 798
- Pérez-González, P. G., Gallego, J., Zamorano, J., & Gil de Paz, A. 2001, *A&A*, 365, 370
- Pérez-González, P. G., Zamorano, J., Gallego, J., & Gil de Paz, A. 2000, *A&AS*, 141, 409
- Pettini, M., Shapley, A. E., Steidel, C. C., Cuby, J., Dickinson, M., Moorwood, A. F. M., Adelberger, K. L., & Giavalisco, M. 2001, *ApJ*, 554, 981
- Pisano, D. J., Kobulnicky, H. A., Guzmán, R., Gallego, J. ., & Bershadsky, M. A. 2001, *AJ*, 122, 1194
- Quirk, W. J. 1972, *ApJ*, 176, L9
- Reynolds, R. J. 1990, in *IAU Symp. 139: The Galactic and Extragalactic Background Radiation*, Vol. 139, 157–169
- Rowan-Robinson, M. 2001, *ApJ*, 549, 745
- Rozas, M., Beckman, J. E., & Knapen, J. H. 1996, *A&A*, 307, 735
- Salzer, J. J., MacAlpine, G. M., & Boroson, T. A. 1989, *ApJS*, 70, 479
- Sandage, A., Tammann, G. A., & Yahil, A. 1979, *ApJ*, 232, 352
- Sauvage, M. & Thuan, T. X. 1994, *ApJ*, 429, 153
- Schmidt, M. 1968, *ApJ*, 151, 393
- Serjeant, S., Gruppioni, C., & Oliver, S. 2002, *MNRAS*, 330, 621
- Somerville, R. S., Primack, J. R., & Faber, S. M. 2001, *MNRAS*, 320, 504
- Songaila, A., Cowie, L. L., Hu, E. M., & Gardner, J. P. 1994, *ApJS*, 94, 461
- Stoughton et al. 2002, *AJ*, 123, 485
- Sullivan, M., Mobasher, B., Chan, B., Cram, L., Ellis, R., Treyer, M., & Hopkins, A. 2001, *ApJ*, 558, 72
- Trager, S. C., Worthey, G., Faber, S. M., Burstein, D., & González, J. J. 1998, *ApJS*, 116, 1
- Tresse, L., Maddox, S., Le Fevre, O., & Cuby, J. 2001, *MNRAS*, astro-ph/0111390
- Vitores, A. G., Zamorano, J., Rego, M., Alonso, O., & Gallego, J. 1996a, *A&AS*, 118, 7

- Vitores, A. G., Zamorano, J., Rego, M., Gallego, J., & Alonso, O. 1996b, *A&AS*, 120, 385
- Wang, J., Heckman, T. M., & Lehnert, M. D. 1997, *ApJ*, 491, 114
- . 1999, *ApJ*, 515, 97
- Yan, L., McCarthy, P. J., Freudling, W., Teplitz, H. I., Malumuth, E. M., Weymann, R. J., & Malkan, M. A. 1999, *ApJ*, 519, L47
- Youngblood, A. J. & Hunter, D. A. 1999, *ApJ*, 519, 55
- Zamorano, J., Gallego, J., Rego, M., Vitores, A. G., & Alonso, O. 1996, *ApJS*, 105, 343
- Zamorano, J., Rego, M., Gallego, J. G., Vitores, A. G., González-Riestra, R., & Rodríguez-Caderot, G. 1994, *ApJS*, 95, 387
- Zurita, A. 2001, PhD thesis, Instituto de Astrofísica de Canarias
- Zurita, A., Beckman, J. E., Rozas, M., & Ryder, S. 2002, *A&A*, 386, 801

Table 2. Results of the H α imaging study of the UCM sample.

UCM name (1)	F (H α) (2)	c_{31} (3)	r_e (4)	$\frac{r_{80}}{r_{24.5}}$ (5)	EW (H α) (6)	(B/T) (H α) (7)	L (H α) (8)	$Area_T$ (9)	Σ_{SFR}^{max} (10)	%DIG (11)	%DIG $_c$ (12)
0013+1942	8.6	2.54	3.1	0.59	113.4	0.14	2.57	70.5	0.498	4	22
0014+1748	13.6	10.99	7.8	0.93	15.6	0.68	5.68	71.2	0.470	32	48
0014+1829	16.6	6.21	2.3	0.65	99.6	0.48	26.26	99.1	0.075	4	24
0015+2212	4.2	3.41	1.0	0.23	35.2	0.48	0.54	29.0	0.037	6	20
0017+1942	11.2	1.88	8.9	0.99	56.1	0.00	4.93	113.3	7.250	4	23
0047+2413	10.7	5.63	6.9	0.49	29.3	0.45	12.66	132.9	0.464	7	23
0047+2414	22.5	3.18	5.5	0.68	62.0	0.05	21.27	241.1	0.368	4	19
0056+0043	5.3	3.37	1.5	0.43	48.5	0.12	0.86	26.8	0.357	2	18
0056+0044	6.6	9.95	4.2	0.99	72.2	0.32	0.57	69.1	0.214	9	39
0141+2220	2.8	4.79	3.0	1.00	18.6	0.31	0.64	26.9	0.213	12	33
0147+2309	4.0	2.01	1.9	0.26	17.5	0.39	0.95	5.4	0.195	0	62
0148+2124	6.5	5.85	1.2	0.74	89.7	0.08	0.57	32.2	0.153	1	28
0159+2326	2.5	2.80	1.1	0.15	7.5	0.14	1.19	15.8	0.150	6	15
1246+2727	10.0	3.05	8.1	0.85	49.5	0.14	3.42	179.0	0.149	7	38
1247+2701	2.5	1.87	3.8	0.62	23.5	0.03	0.40	36.7	36.985	7	36
1248+2912	8.4	5.26	9.1	0.74	13.6	0.41	2.06	118.4	1.686	10	30
1253+2756	19.9	1.58	3.7	0.39	82.0	0.36	1.22	65.9	1.061	1	14
1254+2740	7.9	3.38	2.0	0.40	38.8	0.64	1.26	63.7	1.001	2	25
1255+2819	4.0	1.90	3.3	0.30	16.9	0.22	1.71	54.0	0.875	10	31
1255+3125	8.0	4.10	2.0	0.49	35.7	0.69	2.64	42.7	0.722	2	25
1256+2701	5.2	4.45	8.8	0.99	63.1	0.04	1.16	79.9	0.710	11	49
1256+2722	2.1	3.28	3.5	0.76	22.9	0.07	1.65	29.8	0.443	13	41

Table 2—Continued

UCM name (1)	F (H α) (2)	c_{31} (3)	r_e (4)	$\frac{r_{80}}{r_{24.5}}$ (5)	EW (H α) (6)	(B/T) (H α) (7)	L (H α) (8)	$Area_T$ (9)	Σ_{SFR}^{max} (10)	%DIG (11)	%DIG $_c$ (12)
1256+2910	0.7	2.15	1.2	0.11	2.9	1.00	1.85	8.5	0.432	11	33
1257+2808	1.7	10.99	1.1	0.91	10.0	0.43	0.58	7.6	0.431	12	39
1258+2754	6.8	2.31	4.2	0.50	28.2	0.21	6.21	90.4	0.376	7	26
1300+2907	9.0	3.61	2.4	0.66	155.1	0.52	4.12	16.6	0.317	0	39
1301+2904	12.8	2.45	6.4	0.90	59.8	0.55	2.59	195.2	0.216	15	45
1302+2853	1.8	1.52	2.5	0.32	10.4	0.00	0.55	25.5	1.125	5	11
1303+2908	13.0	1.66	6.9	0.99	170.6	0.00	2.02	78.6	0.805	3	16
1304+2808	7.0	2.75	4.7	0.44	20.7	0.51	0.70	83.7	0.746	8	28
1304+2818	6.4	2.57	5.3	0.55	22.9	0.02	0.95	93.3	0.434	17	58
1304+2830	1.1	2.53	1.3	0.48	47.9	0.24	0.20	12.5	0.130	2	33
1306+2938	14.6	2.04	4.2	0.45	39.1	0.20	3.16	118.3	0.122	4	23
1306+3111	3.2	2.23	2.7	0.36	21.8	0.01	1.59	59.4	0.104	8	23
1308+2950	9.1	10.99	13.9	0.99	9.4	0.55	19.71	41.9	0.063	34	62
1308+2958	9.3	2.34	10.3	0.83	19.0	0.12	5.08	118.8	1.559	24	63
1314+2827	3.9	1.88	1.9	0.17	19.5	0.48	1.87	32.8	1.239	4	15
1324+2651	18.1	3.93	1.6	0.33	41.0	0.89	8.93	81.7	0.613	3	17
1324+2926	6.4	2.46	2.0	0.54	202.6	0.17	0.43	34.5	0.487	0	15
1331+2900	5.3	3.60	1.0	0.72	919.4	0.01	1.56	22.5	0.341	0	13
1431+2854	8.5	2.47	5.3	0.61	31.3	0.26	28.67	127.5	0.250	6	44
1431+2947	3.3	3.10	1.9	0.58	106.3	0.56	0.36	34.2	0.201	5	26
1432+2645	5.9	7.48	8.9	0.45	12.6	0.38	4.77	56.3	0.160	23	41
1440+2521N	2.7	4.91	1.2	0.33	20.7	0.69	2.82	33.6	0.153	17	23

Table 2—Continued

UCM name	F (H α)	c_{31}	r_e	$\frac{r_{80}}{r_{24.5}}$	EW (H α)	(B/T) (H α)	L (H α)	$Area_T$	Σ_{SFR}^{max}	%DIG	%DIG $_c$
(1)	(2)	(3)	(4)	(5)	(6)	(7)	(8)	(9)	(10)	(11)	(12)
1440+2521S	5.0	7.45	4.0	0.99	45.7	0.61	1.85	49.6	0.129	4	49
1443+2548	15.1	3.04	5.4	0.72	59.8	0.04	18.04	201.9	0.129	2	27
1444+2923	4.1	6.22	7.1	0.99	42.1	0.85	1.60	33.6	0.124	17	73
1513+2012	24.0	3.71	2.7	0.42	80.6	0.51	24.00	99.3	0.106	0	15
1537+2506N	17.8	3.96	1.1	0.15	29.8	0.80	4.56	60.0	0.095	4	15
1537+2506S	13.8	3.10	2.5	0.38	63.7	0.39	2.63	65.0	0.082	3	15
1612+1308	8.2	2.98	1.0	0.46	414.5	0.00	0.24	18.4	0.073	0	13
1646+2725	3.3	2.92	2.2	0.99	144.8	0.04	1.69	35.5	0.071	5	25
1647+2727	7.3	2.70	2.5	0.71	84.5	0.36	8.19	56.8	0.064	7	30
1647+2729	14.7	2.51	4.5	0.72	59.2	0.04	22.57	163.2	0.060	3	25
1647+2950	8.1	5.61	3.3	0.44	17.4	0.29	6.98	110.8	0.925	6	28
1648+2855	25.4	1.53	3.5	0.37	78.5	0.22	8.41	123.5	0.696	2	10
1656+2744	3.6	2.80	0.8	0.20	38.0	0.75	2.76	18.7	0.511	10	13
1657+2901	4.5	2.14	3.5	0.81	53.0	0.14	2.85	56.5	0.459	6	26
2238+2308	25.8	2.36	4.8	0.36	31.1	0.13	24.12	134.4	0.444	6	32
2249+2149	4.3	8.07	8.1	0.80	11.5	0.57	36.23	40.8	0.396	16	57
2250+2427	16.2	4.47	1.4	0.35	45.2	0.54	29.43	110.0	0.338	6	7
2251+2352	7.0	2.14	2.2	0.40	48.9	0.10	1.34	49.1	0.325	4	14
2253+2219	9.4	2.72	2.7	0.61	44.5	0.37	3.34	76.8	0.294	2	22
2255+1654	2.6	4.07	5.4	0.83	12.5	0.33	2.12	40.9	0.272	22	50
2255+1926	2.4	5.07	2.3	0.91	26.8	0.12	0.25	19.7	0.261	4	43
2255+1930N	13.7	2.49	2.9	0.28	34.1	0.22	5.08	68.5	0.223	3	12

Table 2—Continued

UCM name	F (H α)	c_{31}	r_e	$\frac{r_{80}}{r_{24.5}}$	EW (H α)	(B/T) (H α)	L (H α)	$Area_T$	Σ_{SFR}^{max}	%DIG	%DIG $_c$
(1)	(2)	(3)	(4)	(5)	(6)	(7)	(8)	(9)	(10)	(11)	(12)
2255+1930S	8.1	2.72	2.5	0.49	39.3	0.19	1.48	74.8	0.191	5	21
2258+1920	10.4	2.68	4.7	0.58	35.6	0.05	1.79	102.0	0.178	3	16
2304+1640	3.6	2.55	1.8	0.52	101.9	0.00	0.52	30.8	0.175	3	26
2307+1947	3.9	9.41	1.4	0.79	21.5	0.39	1.06	38.0	0.170	16	34
2313+2517	11.9	7.70	3.8	0.44	11.1	0.44	13.87	94.0	0.164	0	27
2315+1923	5.3	3.50	0.9	0.30	96.8	0.76	5.94	24.0	0.159	4	12
2316+2457	35.5	7.34	7.6	0.56	30.8	0.38	23.09	290.3	0.156	6	17
2316+2459	6.7	4.74	6.6	0.54	21.2	0.34	13.55	90.7	0.141	15	37
2325+2318	150.9	2.32	8.9	0.64	72.5	0.00	11.39	619.3	0.140	0	9
2326+2435	13.6	4.65	3.8	0.71	100.4	0.27	1.71	86.5	0.138	5	17
2327+2515N	8.8	4.90	1.8	0.48	49.6	0.00	1.61	25.6	0.133	0	29
2327+2515S	21.0	2.90	1.7	0.22	86.2	0.00	6.39	35.1	0.132	0	14
2329+2427	2.0	9.93	1.4	0.53	3.8	0.66	3.99	15.1	0.121	14	42

Note. — Results of the H α imaging study. Columns stand for: (1) UCM name. (2) H α flux corrected for N II contamination in units of 10^{-14} erg s $^{-1}$ cm $^{-2}$. Median error is 16%. (3) Concentration index c_{31} . Median error is 8%. (4) Effective radius in arcsec. Median error is 7%. (5) Ratio between the H α emitting region (radius of the circular region containing 80% of the total H α emission) and the entire galaxy sizes (radius of the 24.5 mag arcsec $^{-2}$ in the R $_C$ band). Median error is 17%. (6) Equivalent width of the H α image in Å. Median error is 17%. (7) Bulge-to-total luminosity ratio of the H α emission. Median error is 13%. (8) H α luminosity corrected for internal extinction. Units are 10^{41} erg s $^{-1}$. Median error is 16%. (9) Area of the emitting region (square arcsec). (10) Maximum star formation rate density observed in \mathcal{M}_\odot yr $^{-1}$ kpc $^{-2}$. Median error is 16%. (11) Percentage of the DIG emission to the total H α flux. Median error is 14%. (12) The same as (11) but corrected for the DIG overimposed in the star-forming knots.